8-24-2012

The Role of Transport Phenomena in the Direct Oxidation of Solid Fuels

Charles J. Banas
University of Connecticut - Storrs, banas.charles@gmail.com

The Role of Transport Phenomena in the Direct Oxidation of Solid Fuels

Charles Joseph Banas

B.S.E., University of Connecticut, 2010

A Thesis

Submitted in Partial Fulfillment of the

Requirements for the Degree of

Master of Science

at the

University of Connecticut

2012

APPROVAL PAGE

Master of Science Thesis

The Role of Transport Phenomena in the Direct

Oxidation of Solid Fuels

Presented by

Charles Joseph Banas, B.S.E.

Major Advisor _____

Ugur Pasaogullari

Associate Advisor _____

Prabhakar Singh

Associate Advisor _____

Zhuyin Ren

University of Connecticut

2012

Acknowledgements

This work was supported by the U.S. National Science Foundation (CBET-0748063) and the U.S. Department of Education Graduate Assistance in Areas of National Needs (GAANN) P200A070354.

I would like to than my major advisor Ugur Pasaogullari for his patience and guidance during my time at C2E2. His leadership and understanding through good and bad times cannot be recognized enough. I would also like to thank Prabhakar Singh and Zhuyin Ren for their presence and support during my defense. Dr. Singh and Dr. Ren's efforts during my final days at C2E2 are appreciated. I thank my lab colleague Phillip Baker, who helped me learn the proper fuel cell assembly and testing protocol, along with Pete Menard and Garry Barnes, and numerous other students and staff who had time to answer my questions. I would also like to thank my colleagues and friends Justin Roller and Omer Selamet who were always available for guidance and support during my time at C2E2. And lastly, I would like to thank my parents, family, and friends for their unwavering support over the last 23 years.

Table of Contents

Nomenclature

A	Area (cm^2)
C_p	Specific heat (J/kg-K)
$C_{s,f}$	Coefficient of the Rohsenow Pool Boiling Correlation
d	Diameter (cm)
ECSA	Electrochemical surface area
F	-Faraday's Constant (96485.3C/mol e^-)
	-Force (N)
f	Cell face volume fraction
g	Gravitational acceleration
h	Height
h_{lv}	Latent heat of vaporization (J/kg)
I	Current (A)
j	Current density (A/cm^2)
l	Length (cm)
M	Atomic weight (g/mol or kg/kmol)
$\dot{m}$"	Mass consumption/production flux ($g/s\text{-}cm^2$)
m''	Mass flux ($g/s\text{-}cm^2$)
$\dot{m}$	Mass transfer rate (kg/s)
N	Number of particles
n	-Number of electrons per 1 molecule of species
	-Coefficient in Rohsenow Pool Boiling Correlation
	-Total number of phases modeled in the VOF model
	-Current time step
$\dot{n}$"	Molar consumption/production flux ($mol/s\text{-}cm^2$)
$\vec{n}$	Gradient of volume fraction
$\hat{n}$	Unit normal gradient of the volume fraction
P	Pressure (Pa)
Pr	Prandtl number
q''	Heat flux (W/cm^2)
R	Radius (cm)
	Gas Constant
S	Source term ($kg/s\text{-}m^3$)
T	Temperature (K or °C)
t	Time (sec)
Δt	Time step (sec)
U	Velocity component (cm/s)
V	Volume (cm^3)

$\vec{V}$	Velocity (cm/s)
w	Width (cm)
α	Phase volume fraction
ζ	Roughness correction
θ	Contact angle (°)
κ	Surface curvature (cm^{-1})
μ	Dynamic viscosity (Pa-s)
π	Pi (3.14159)
ρ	Density (kg/m^3)
σ	Surface tension (N/m)
τ	Shear stress (Pa)
ϕ	Cavity half angle (°)

Subscripts

a	advancing (see contact angle)
b	base
buoy	due to buoyancy
c	covered area
cap	reference to spherical cap
CFD	Virtual surface area/volume
E	east
f	cell face
h	horizontal
l	liquid
N	north
o	initial
p	primary phase
q	secondary phase
S	south
W	west
s	supplementary
sat	saturation
tot	total
v	vertical
	vapor
w	wall/surface
σ	due to surface tension

List of Figures

Abstract

Direct carbon fuel cells have shown promise for stationary power generation by utilizing the direct oxidation of a solid carbon fuel source at the anode. In laboratory settings, researchers have reported up to 300mA/$cm^2$of current density from these cells types which suffer from mass transport losses. This paper studies the surface properties of the solid fuel source, and describes the process of CO_2 evolution through an analogy to pool boiling. In nucleate boiling (a subset of pool boiling) vapor bubbles grow from nucleation sites where gas are trapped in micro-cavities on the surface. Carbon surfaces possess these same features, entrapping gases when they are immersed in a liquid electrolyte. The geometric shape and departure radius of these bubbles are shown to be different depending on the surface wetting characteristics. A force balance is performed to equilibrate the buoyant and surface tension forces as a function of contact angle, showing that CO_2 gas bubbles requires significant volume to depart the carbon surface, a problem which robs the fuel source of electrochemical surface area. To confirm these findings, ANSYS FLUENT is utilized to show the growth rate and shape of CO_2 bubbles on the surface of carbon. The results show that carbon particles inside the anode of a direct carbon fuel source can be encircled by a film of CO_2 gas rendering them inactive.

1. Introduction

Rich abundances of coal are available throughout the world, and especially in industrial nations such as the United States. Current estimates show that roughly a quarter of world's energy production is tied to the use of coal, and that number is projected to rise to 28% within the next 20 years (Li et al., 2010a). The result of this continued use is the exhaust of endless streams of carbon dioxide (CO_2) and various other greenhouse gases that are released into the atmosphere. In an effort to reduce pollutant emissions, fuel cells have become a possible alternative to the traditional power generation through the burning of coal. However, many of these stationary cell types (those suitable for large scale power generation) that have been developed involve breaking down a hydrogen containing compound. This fuel is supplied either as hydrogen gas or a hydrocarbon to generate electricity. Direct Carbon Fuel Cells (DCFC) offer a cleaner alternative to combusting coal, and do not require a change in fuel infrastructure, as they can operate on the same fuel already in use, coal.

The history of DCFC's dates back to the 19^{th} century, yet the fundamental chemistry and physics have only been understood within the past two decades. Cao et al. (2007) describes the first attempts at converting carbon to electricity, beginning with the electrochemical cells of Jablochkoff (1877) and Bacquerelle (1985). These cells used carbon at the anode, an iron (Fe) - platinum (Pt) cathode, with an electrolyte consisting of potassium nitrate (KNO_3). While these cells could produce current, the choice of KNO_3 as an electrolyte caused the cell to be unstable, thus dooming these designs to failure. Shortly after Bacquerelle's cell was introduced, Jacques (1896) created a new cell design, labeled by Cao as possibly the "first DCFC." At the anode, coal rods were placed in a

molten sodium hydroxide (NaOH) electrolyte which was heated to 400-500°C. By passing air through the cathode, a current of 100mA/cm^2 was reported to have been drawn, with a total power generation rate of 1.5kW in a 100 cell stack. However, the chemistry of this cell was not entirely understood, with the overall reaction believed to consume the electrolyte in an irreversible battery-like reaction. Due to the advances in the steam generator, and the lack of repeatability in Jacques' design, the development of DCFC's stopped for more than a century.

As early as 1935, Tamaru et al. experimentally proved that the electrochemical oxidation of carbon was possible at 700°C with the dominant product of CO_2 (Cao et al., 2007). The overall reaction is shown in the following equation, which has a theoretical potential of 1.02V (Cooper, 2004):

$$C + O_2 \rightarrow CO_2 \quad (1)$$

Later work by Vutetakis et al. (1987) showed that carbon derived from coal could be oxidized, and confirmed that CO_2 was the main product at large overpotentials, while higher concentrations of carbon monoxide (CO) would be produced at low overpotentials. Today research continues in the development of DCFC's to improve the cell design and performance at places like the Lawrence Livermore National Laboratory (LLNL) (Cooper, 2004). Due to the numerous advantages that they offer, DCFCs have the potential to become a viable alternative to coal fired power plants, if the technical challenges are resolved.

One of the biggest advantages to optimizing the performance of a DCFC is the availability and energy density of its fuel. The carbon fuel can come from almost any carbon containing fuel, including petroleum, biomass, graphite, natural gas and coal

(Cherepy et al., 2005). When compared to other fuels that are used in fuel cells, carbon has the highest energy per unit volume, as is shown in Table 1. Because carbon is in the solid phase, this gives the DCFC the ability to produce much energy in a small volume.

Table 1: Energy Densities for Common Fuel Sources (Cao et al., 2007)

Fuel Source	Energy Density (kWh/L)
Carbon	20.0
Hydrogen	2.4
Methane	4.0
Gasoline	9.0
Diesel	9.8

If carbon derived from coal were to be used, then the abundant coal reserves of many countries could be utilized in DCFCs, which is not limited by the Carnot (i.e. heat engine) efficiency. Because electricity is generated by an electrochemical reaction that does not require combustion and conversion of chemical energy into thermal energy, the theoretical efficiency is not limited by the operating temperature as dictated by Carnot. Instead, due to the small entropy change and anode stability, voltage efficiencies of up to 80% have been achieved using a fuel derived from coal as the anode fuel source. Also contributing to this high efficiency is that in theory, the entire carbon structure can be consumed without complex recirculation requirements. This is higher than either hydrogen or methane in which can be as low as 80% of the fuel is utilized in a fuel cell without recirculation, as reported by Cooper (2004).

While high efficiency and the availability of fuel are the advantages to developing a DCFC, implementation of this technology must overcome issues including ones related to performance. The greatest hurdle to overcome is that, while current can be drawn from fuel derived from coal; DCFCs' performance still needs to be improved. Cooper (2004) and Cherepy et al. (2005) have published results showing that coal can produce current

densities up to 120mA/cm^2, while other carbon containing fuels have reached 300mA/cm^2 at 800mV of anode overpotential. Much of the performance loss can be contributed to the kinetic and mass transport losses that are seen with these cells. The electrochemical oxidation of carbon into CO_2 is a kinetically slow process that requires high temperatures to improve the reaction rate. Mass transport losses are also observed as many cell designs are now optimized to improve the mass transport of both the reactant carbon and product CO_2. An additional problem involves the logistics of refueling. Laboratory scale cells have had little ability to refuel, outside of shutting down the cell to physically reintroduce carbon to the process. Another problem is with electrical conductivity. In an effort to reduce ohmic resistance, carbon should be in good electrical contact with the current collector, and if this contact is lost electron transport to the current collector will be hampered. Other unresolved issues include impurities of the carbon fuel, although there is debate as to whether the impurities significantly affect the rate of the electrochemical reaction, but it is certain that impurities contaminate the electrolyte and degrade cell components to the point where they need to be replaced (Cooper, 2004).

Successful demonstration of this technology would effectively double the Earth's coal reserves (Cooper, 2004). For each of the challenges presented above, there are current efforts to resolve the issues; however it is seen that there is a lack of current understanding about the transport phenomena that occurs in the anode. Cherepy (2005) and Vutetakis (1987) have developed new cell designs to improve the transport of carbon within the electrolyte solution. Li et al. (2009) has modified the carbon surface to increase the cell's performance by altering the surface structure and chemistry of carbon.

But there is no proposed theory as to what actually occurs inside the anode of a direct carbon fuel cell. This thesis introduces a phenomenological model to explain the physics of mass transport in DCFCs and associated performance, which are shown in the chapters of *Physical Model* and *Volume of Fluid (VOF) Model for CO_2 Gas Formation*. The next section, however presents an overview of what is known about the DCFC technology.

2. Background

The driving force behind the development of DCFC's is to develop a fuel cell that is able to use an abundant natural resource (i.e. coal) as its primary fuel. As was shown in Eq. 1, the overall reaction ideally combines carbon and oxygen to produce carbon dioxide. This would theoretically be pure carbon dioxide at the anode outlet that could be then captured for other uses, such as recovering oil from beneath the Earth's surface (Cao et al., 2007). In the cathode, oxygen, carbon dioxide, and electrons are combined to form the carbonate ion as shown in Eq. 3. Carbonate ions then migrate to the anode where it reacts with carbon rich fuel according to Eq. 2. In the process, for each carbon atom consumed, four electrons (e^-) and three CO_2 molecules are produced. Combining the individual reactions produces the overall reaction which is shown in Eq. 1 (Cooper, 2004).

Anode Reaction $$C + 2CO_3^{2-} \rightarrow 3CO_2 + 4e^- \quad (2)$$

Cathode Reaction $$O_2 + 2CO_2 + 4e^- \rightarrow 2CO_3^{2-} \quad (3)$$

As Cherepy et al. (2005) has shown many different types of carbon rich fuels can be used in the anode as the fuel. When a solid fuel such as coal is placed in the anode compartment, it usually is first crushed into particles that range in size from tens of nanometers to a couple of millimeters. These are placed in an electrolyte consisting of molten carbonates, molten hydroxide, or a YSZ-based solid (Cao et al., 2007). The choice of electrolyte alters the kinetics of the electrochemical steps, but has little impact on the overall operation of the device. The choice of electrolyte is not studied in this thesis for two distinct reasons. First, much of the current research is conducted using a molten carbonate electrolyte, which will be assumed throughout this paper. Second, for liquid

electrolytes, the governing physics is identical regardless of the electrolyte type, except for the electrolyte properties (such as density or solubility of CO_2).

By assuming the presence of a molten carbonate electrolyte, the chemical steps involved with the production of CO_2 can be studied. The slow kinetics of the oxidation of carbon is only partially understood, because currently an absolute method to determine the intermediate reaction steps, products and reactants in a molten carbonate solution does not exist (Cao et al., 2007). Muthuvel et al. (2009) reports that there are research groups operating DCFC's in the 100°C range, however, most research is conducted between 500-900°C due to the improved activity at those temperatures. Cooper (2004) has reported that some cells have even been operated at temperatures as high as 1100°C. There are six proposed steps that are believed to occur in the process that oxidizes carbon into CO_2 at the anode. The disassociation of the carbonate ion into carbon dioxide and an oxide ion was reported by Vutetakis (1987).

$$O^{2-} + CO_2 \leftrightarrow CO_3^{2-} \tag{4}$$

Cooper (2004) presents the proposed theory of carbon oxidation once the oxide ion is present. This process is shown in Eq. 5-10, and described here. The first step, involves the adsorption of an oxide ion onto the surface carbon atoms, as shown in Figure 1.

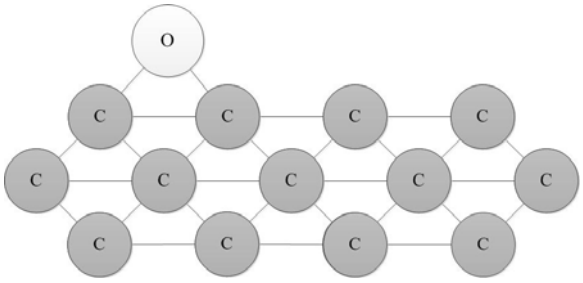

Figure 1: The adsorption of the oxide ion onto the surface of carbon

After the oxide ion is attached to the surface, the next two steps involve discharging the electrons from the surface, which would in turn be transferred to the current collector. This forms what Cao et al. (2007) calls a "C-O-C bridge" (C_2O) on the surface. Once this is formed, it allows another oxide ion to adsorb into the "bridge" to form a "C-O-C-O-C bridge" (C_3O_2), which is the slowest process and thus the rate determining step. This "bridge" is shown in Figure 2.

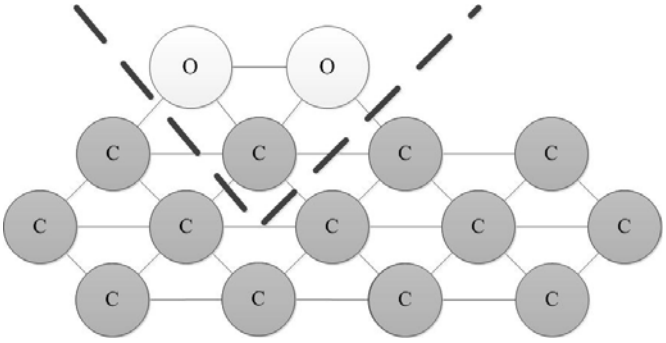

Figure 2: The adsorption of the second oxide onto the carbon surface to form the C_3O_2 bridge

After this second oxide ion attaches, the remaining two steps involve discharge of the last two electrons. Once the last electron is removed, then the CO_2 molecule is released from the surface and enters into the electrolyte solution. Each of these steps is shown in Equations 5-10.

$$C_{sur} + O^{2-} \rightarrow C_{sur}O^{2-} \quad (5)$$

$$C_{sur}O^{2-} \rightarrow C_{sur}O^{-} + e^{-} \quad (6)$$

$$C_{sur}O^{-} \rightarrow C_{sur}O + e^{-} \quad (7)$$

$$C_{sur}O + O^{2-} \rightarrow C_{sur}O_2^{2-} \quad (8)$$

$$C_{sur}O_2^{2-} \rightarrow C_{sur}O_2^{-} + e^{-} \quad (9)$$

$$C_{sur}O_2^{-} \rightarrow CO_2 + e^{-} \quad (10)$$

While this is the theory behind the operation of DCFC's, the resulting physics does not always operate according to what is proposed to happen. One of the first

problems that is encountered, is that with the high operating temperatures, there is the possible formation of carbon monoxide (CO) because at temperatures above 750°C, the Boudouard reaction begins to occur (Cao et al., 2007). Initially thought to be the dominant reaction for the oxidation of carbon (instead of Eq. 1), the Boudouard reaction results in only one or two electrons being transferred from a carbon atom instead of the four electron process previously described (Li et al., 2010b). The resulting overall Boudouard reaction is shown in the Eq. 11, while the two possible corresponding anode reactions are shown in Equations 12 and 13:

$$C + CO_2 \rightarrow 2CO \tag{11}$$

$$C + CO_3^{2-} \rightarrow CO_2 + CO + 2e^- \tag{12}$$

$$2C + CO_3^{2-} \rightarrow 3CO + 2e^- \tag{13}$$

Through Vutetakis' work, it has been shown that carbon monoxide was not the primary product (1987). While operating at temperatures up to 900°C, Vutetakis reported that the dominant product was CO_2 and that the ratio of CO to CO_2 decreased as the overpotential was increased. Cao et al. (2007) further extends notion, when he writes that for temperatures over 700°C, the dominant product is CO_2 when the overpotential is greater than 100mV.

With the general theory of kinetics behind DCFC's presented, the following discussion pertains to the engineering of the actual fuel cell. This includes, designing the cell, choosing the appropriate materials, preparing the fuel, and experimentally testing the cell. First, an analysis of cell designs will be given to show how DCFC's operate and what changes have been made to improve cell performance. The first cell design to be described will be the simplest design which is based on a flat plate. This design was used

by Cherepy et al. (2005) to study the performance of different carbon containing fuels in a laboratory setting. This design is shown in Figure 3.

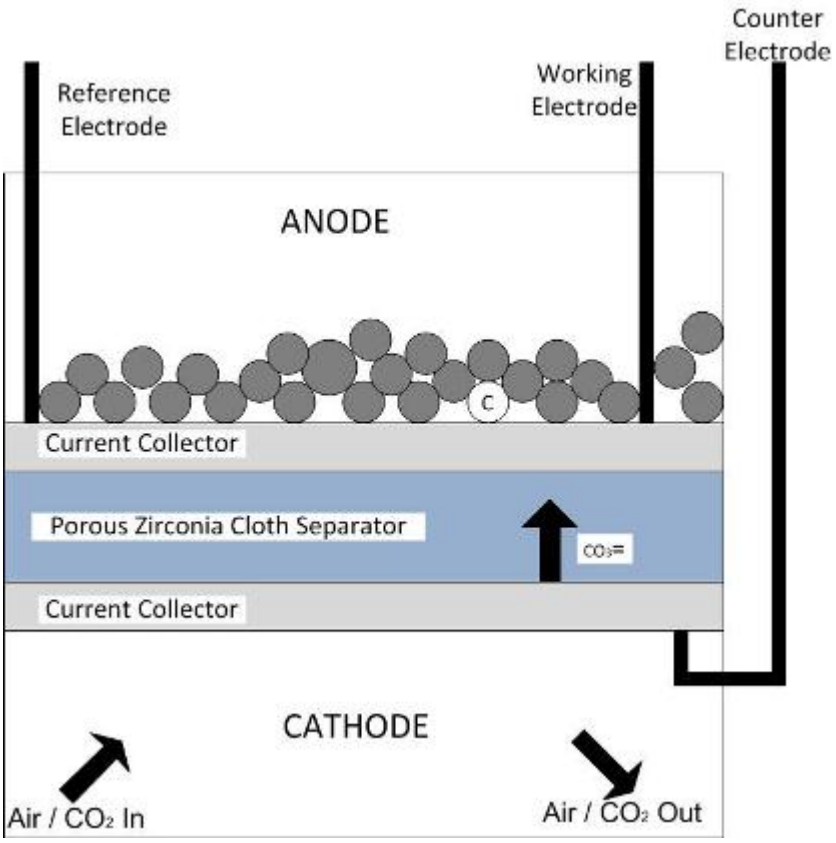

Figure 3: Flat plate design used for laboratory scale testing

This design had a flow pattern to allow air and CO_2 to enter the cathode. The electrode consists of a porous nickel material supported by a stainless steel backing. This porous material allows for the passage of carbonate and acts as a current collector for the electrons transferred in the reaction. Once the carbonate ion is formed, it passes through a porous zirconia cloth, with a thickness of 760µm (Cherepy et al., 2005) saturated with molten carbonate solution. This acts as a separator between the anode and cathode, and prevents crossing of electrons. Once through the zirconia cloth, the carbonate ion enters another porous nickel structure before leaving and reacting with the carbon particles in

the anode. An argon stream is passed through the anode to prevent the introduction of air to the anode mixture and help carry away the product CO_2 (Cherepy et al., 2005).

This flat plate design is useful in laboratory settings only. The design has a geometric surface area of just 2.8cm^2, while having no provisions for refueling or enhancing mass transfer. However, this setup was not designed for large scale power generation, and will be revisited later in §*3.2 Determination of the Electrochemical Surface Area and CO_2 Evolution Rate*. To improve the distribution of carbon throughout the anode compartment, two different cell designs have been created. The first of these designs involves a stirring rod placed in the anode compartment, as is visible in Figure 4.

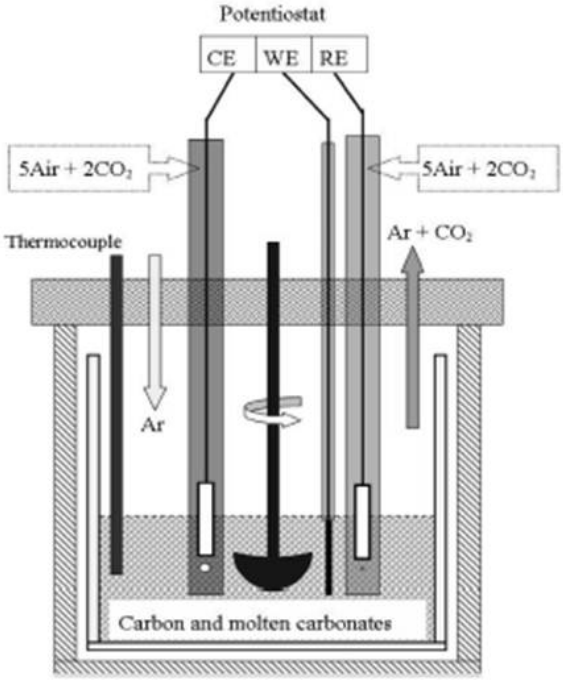

Figure 4: DCFC with a stirring rod for improved mass transport from Li et al. (2010a)

This design was used by both Vutetakis (1987) and Li (2010a) in their experiments studying the oxidation of carbon fuels. In this design, air and CO_2 are passed through the cathode tube, which is impermeable to the carbon fuel. A stirring rod is located at the center of the cell to increase the amount of carbon at the working electrode. However,

this is not practical to scale up due to its cumbersome nature. In an effort to create a DCFC that is suitable for large scale power generation, Cooper (2004) reports that scalability should be incorporated into the design of new DCFC's. In the third type of cell design, the mass transfer enhancing properties of the stirring rod are combined with the simplicity of the flat plate design.

As part of his work, Cooper (2004), along with Cherepy et al. (2005), has proposed a new DCFC design that is simple, yet has the ability to scale up, while using the exact same materials as the flat plate design. In the laboratory setting, this design had a geometric surface area of 60cm^2 with the potential to scale up to industrial standards. This is shown in Figure 5, as the inclined plate design.

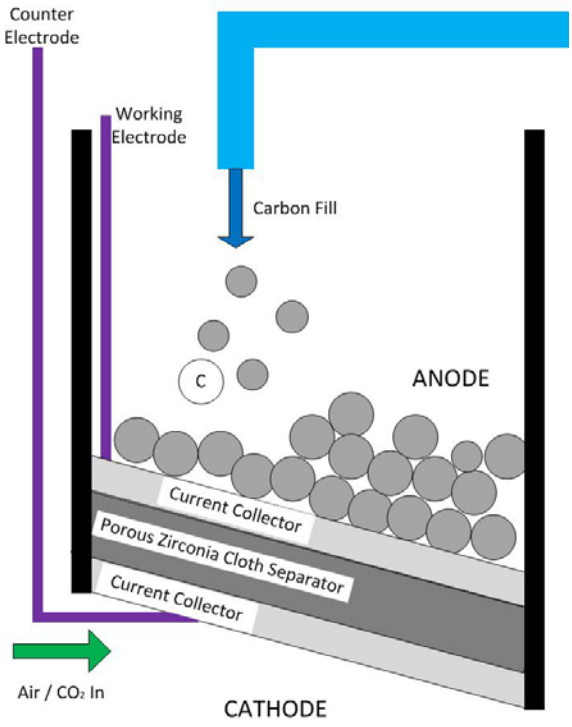

Figure 5: Inclined plate design used in laboratory settings, with possible scale up potential

This design solves three major problems that had occurred with previous designs. First, it includes a carbon fill tube to allow for a continuous flow of carbon particles during

operation. It also is tilted at an angle between 5-45°, which is of the operators choosing. This tilt allows for the electrolyte to be able to drain out of the cell to avoid a buildup of electrolyte and shortage of carbon. And lastly, it involves only simple changes to the flat plate design, which means that the angled inlet design could be scaled up to meet industrial needs.

With several cell designs described, the anode compartment itself can be explored. When using a solid fuel, such as coal, large natural samples are not used in the cell. Instead, the large carbon containing material is crushed into smaller particles. The size of the particle varies. Cherepy et al. (2005) crushed carbon samples down to diameters ranging from tens of nanometers to hundreds of micrometers. Li et al. (2010a) experimented with coal samples around 1-2mm. No research could be found that has studied the effect of particle size.

As previously stated, the carbon fuel can be derived from any fuel source. Cooper (2004) and Cherepy et al. (2005) conducted experiments at Lawrence Livermore National Laboratory (LLNL) to measure the performance of selected carbon rich fuels. Using the flat plate cell design with an operating temperature of 800°C, nine different carbon containing solids were placed in a molten carbonate electrolyte (32% Li_2CO_3 – 68% K_2CO_3) to measure the current density (based on the geometric surface area) at 0.8V. The results from this experiment are shown below in Table 2:

Table 2: DCFC performance dependent on carbon rich fuel source

Carbon Rich Fuel	Current Density at 0.8V
Graphite Particles	58
Calcined Petroleum Coke	58
Acetylene Black	77
Furnace Black	110
Coal Derived Activated Carbon	65
Coconut Activated Carbon	102
Peach Pit Tar	124
Aerogel Carbon	87

From this table, a number of conclusions can be shown. First, a wide variety of carbon containing materials can be added to the anode compartment to operate a DCFC. However, the choice of the carbon source affects the reaction rate. Carbon derived from peach pits and coconuts, along with furnace black carbon produced the highest current densities at this potential, while graphite and coal produced significantly less power. Li et al. (2010a) confirmed the fact that DCFC's operating on coal do not provide high levels of performance. This group took four different coal samples from Australia and ran them through a DCFC to examine the resulting polarization scans. These four samples were labeled Blackwater (BW), Kinston (KT), Newland (NL), and Germancreek (GK), which are all coals from Queensland, Australia. The polarization scans are shown in Figure 6.

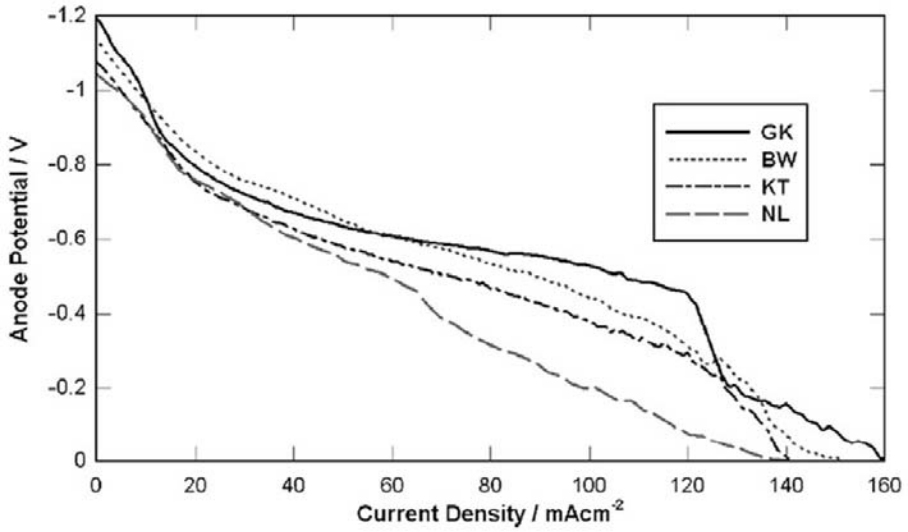

Figure 6: Anode potential of DCFC's comparing the performance differences of coal types (Li et al., 2010a)

From these scans, much worse performance is shown than was reported by Cherepy et al. (2005), with roughly a third of the power being produced in this work at the same level of overpotential. It should be noted that this group was not looking to optimize performance but to judge the effects that the coal structure and composition has to identical experiments. This led to the study of the atomic structure and surface chemistry and their effects on DCFC performance. Here it was concluded that the coal composition, surface area, and the number of surface oxygen functional groups were among the important factors to improve performance (Li et al., 2010a).

The work of Li et al. (2010a) is not the only literature to examine the carbon chemistry's influence on performance. Other works by Li et al. (2009 and 2010b) looked at surface modifications to improve performance, while Cao et al. (2007), Chen et al. (2012), and Cooper (2004) have each listed several factors of the carbon surface and structure that have an influence on performance. Among the important factors are surface properties and electrical conductivity. Electrical conductivity is an important factor in carbon choice is in that for electrons to pass from the reaction sites to the current

collector, a high electronic conductivity is required of the carbon to reduce the effect of ohmic polarization losses. The higher the resistance of the carbon, then the higher the ohmic losses observed. The surface factors that influence the reaction rate are more detailed and specific, depending on the surface area, crystal structure, and composition (Cao et al., 2007).

It is virtually universally agreed that the structure of the carbon has a large influence on the performance of the cell. Cao et al (2007), Chen et al. (2012), Cherepy et al. (2005), Cooper (2004), and Li et al. (2010a) all report that the more disordered the carbon is, then the higher the reaction rate. This is because high lattice disorder allows for many surface defects that equate to a large number of reactive sites. However the influence of surface area only is debatable. Initially during the 1970's, Weaver (as reported by Cooper, 2004) reported that high surface area improved the reaction rate. This was refuted in 2004 by Cooper, who found no correlation between surface area and the rate of reaction. As recently as 2010, Li et al. (2010b) could not definitively say whether surface area had a major influence on the oxidation rate.

Impurities were also examined to determine their how they affect cell performance, and if fuel purification/clean-up is necessary. Cooper (2004) contradicts in describing the effect of impurities, where, in the same paper, he states that impurities do and do not have an effect on the reaction rate. Li et al. (2010a) have suggested that impurities may induce side reactions that reduce the cell's lifetime, while Vutetakis (1987) observed a drop in performance at high overpotentials due to foreign materials in coal. The main problem with impurities though, is the presence of sulfur, which is one of the main causes for performance losses during the life of the DCFC. Again, this is a

universally held principle, even by Cooper (2004), that the presence of sulfur degrades the surface of the current collector by the formation of nickel sulfide (NiS). This reduces the electrode surface area, which in turn reduces the area for the carbon particles to transfer electrons, as they must have direct contact with the nickel. Should this occur, the cell resistance greatly increases and performance drops.

By studying these effects, there are two different approaches to improving performance: cleaning and pretreating the carbon substance, or modifying the surface chemistry. By cleaning and pretreating the fuel source, impurities are removed in an effect to improve cell performance and durability. Modifying the surface involves physically changing the surface chemistry to improve the reaction rate. Cooper has described several techniques which involve the use of water or solvents to clean the surface of the carbon, along with other thermal techniques to improve the purity of the carbon source. Li et al. (2009 and 2010b) have looked at several techniques to improve the reaction rate by changing the surface chemistry. For tests samples, which included coal, different treatments were applied to the surface in an attempt to increase the amount of surface oxygen containing groups and electrical conductivity. From these results it was found that by immersing the carbon material in acid, the reactivity of the carbon could be increased, especially when immersed in nitric acid (HNO_3). This was attributed to an increase of surface oxygen, but did not show any effect on long term durability of the cell.

3. Physical Model: Analytical Results

3.1 Problem Statement

Thus far, it has been shown that DCFC's can use a wide variety of fuels, including an abundant natural resource, coal. The main product is shown to be CO_2 in an electrochemical reaction that is kinetically slow, with high mass transport losses. A cell design (the angled plate design by Cooper, 2004) has been proposed that allows for the possibility of scaling up. Techniques to preprocess the carbon fuel, or even fabricate new exotic carbon fuels, have been proposed to improve cell performance. But it seems that there is still no fundamental understanding of the physics occurring within that cell. Researchers produce data on surface topology, crystalline structure, composition, and adsorption rates, all to run their carbon samples through a series of polarization scan to determine which of their samples produces the best performance based on the experimental results, without a thorough understanding of the governing physics.

It has also been known as far back as 25 years ago during Vutetakis' experiment, that there are significant mass transport losses in the system, enough to require a redesign of the actual cell (hence the addition of the stirring rod). Yet since that time, there has been little to no work in understanding where the mass transport losses come from. In various published works, mass transport losses that are known to exist; Li et al. (2010a) specifically states that the stirring rod cell design was used to "improve mass transport at the electrode surface," but then neglects these effects in an effort to examine the kinetics of carbon oxidation, even at high overpotentials. Some papers have gone as far as implying that wetting behavior influences the performance of DCFC, but few have attempted to explain the phenomena. The work of Hong and Selman (2004) has gone the

farthest, indicated that the performance is linked to the wetting behavior. This work attempts to explain the physics within the DCFC from a fundamental standpoint.

Based on the lack of basic understanding of the transport phenomena inside the anode compartment of the DCFC, a model which describes the growth of CO_2 gas is presented. This model begins with a study of the carbon surface, which shows that carbon is non-wetting (Chen, 2012), and often times can be very rough. While Cao et al. (2007) has shown that carbon with high amounts of surface defects produce the highest cell performance, these may allow for trapped gases to initiate a nucleation process which would allow CO_2 gas form bubbles on the surface.

Specifically, when coal is considered, there exists an elaborate pore structure (Botsaris, 1989) where the electrolyte is unable to penetrate. When coal or another carbon source is used, and these types of surfaces are immersed in the molten electrolyte, initially there exists a trapped gas volume within the particle and on the surface of the carbon, where the cavity angle does not allow penetration of the electrolyte. This theory has been written about by Webb (1994), and is illustrated in Figure 7 below.

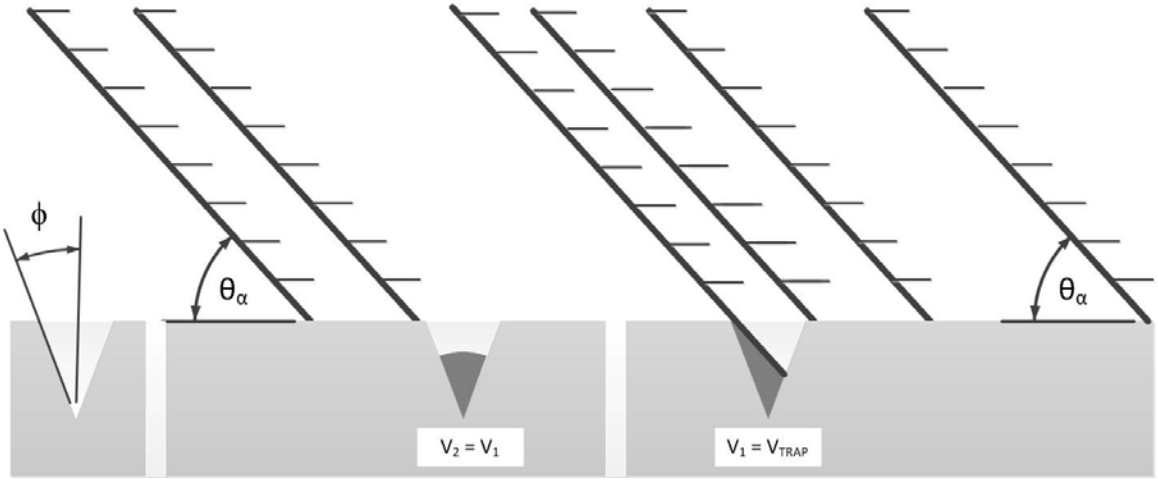

Figure 7: Gas bubble trap as the liquid advances (right) and the resulting trapped bubble (left)

In this figure, a fluid is passed over a surface cavity with a half angle of ϕ. The fluid advances on the solid surface at an angle of θ_a, advancing contact angle. The advancing contact angle is different than the receding contact angle, both of which are different than the static contact angle, i.e. contact angle hysteresis. If the advancing contact angle is greater than the total angle of the cavity ($\theta_a > 2\phi$), then a trapped gas pocket will remain inside the cavity after the fluid has passed over the surface. These gas pockets provide preferential sites for CO_2 bubbles to nucleate, grow, and form larger gas bubbles. During continuous CO_2 evolution, the gas bubbles grow and depart continuously; however preferential nucleation sites will still contain trapped gas pockets following the departure. Figure 8 shows a relatively large slab of graphite that was oxidized in a molten carbonate electrolyte. There exist three small craters that were formed during oxidation. We believe that these craters are the remnants of what were carbon dioxide gas bubbles. These were formed as the concentration of CO_2 exceeded the solubility in the molten carbonate electrolyte, and evolved into gas bubbles. On the nucleation sites (potentially the sites of these craters), CO_2 gas bubbles were formed and allowed to grow to significant size (≈0.25mm in diameter) before departing from the surface. This in turn limits the electrochemical surface area for the reaction to proceed, thus reducing the performance of the cell. Performance will continue to decrease until the large CO_2 bubbles are removed from the surface, freeing it for direct electrochemical oxidation.

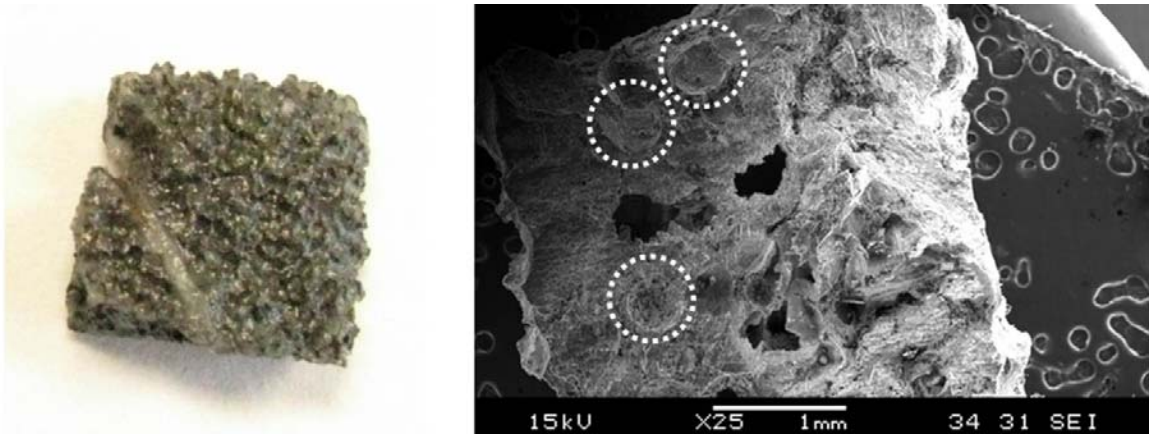

Figure 8: Graphite sample that was oxidized in a molten carbonate electrolyte (left) and an SEM image of the surface (right). Note the distinct crater shapes ≈0.25mm in diameter.

Previously, Chen and Selman (2010) have developed a model that considers the presence of CO_2 gas in the electrolyte solution. This work, different than Chen and Selman considers the origin of those bubbles, beginning with gas pockets that exist once the carbon surface is wetted with the electrolyte. These bubbles are shown not only to have the ability to grow, but also require significant amounts of surface area and volume depart. ANSYS FLUENT (shown in Chapter 4) is used to provide numerical evidence of this phenomenon in an attempt to bridge the gap between fundamentals and experimental results.

3.2 Determination of the Electrochemical Surface Area and CO_2 Evolution Rate

To study the physics of CO_2 bubble growth and possible departure, the first step is to accurately determine the rate of the reaction at the surface. In electrochemical devices, the total amount of electrochemical reactions (i.e. the current) is dependent on the reaction surface area. Since there is no catalyst in a DCFC anode, the amount of area available for the reaction, i.e. electrochemical surface area, is computed by summing the

surface area of all the carbon particles that are currently active in the oxidation process. However, this value is impossible to calculate for a variety of reasons, so researchers commonly replace this area with another value when calculating quantities like the current density. The most common replacement for the electrochemical surface area is the geometric area of the working electrode. While the overall production and consumption rates can be calculated from these measurements, it lacks insight into the fundamental processes at work. Further insight can be obtained by understanding the true electrochemical surface area, and its effect on the rate at which CO_2 is produced, which is important information for Computation Fluid Dynamics (CFD) analyses. To do this, the work of Cherepy et al. (2005) is reanalyzed.

As shown previously in Table 2, several different carbon containing materials were placed in a 2.8cm^2 flat DCFC, and then operated at 0.8V to measure the performance of each of the selected fuels. While the flat plate cell design does not aid in mass transport, to operate at 0.8V provides good insight into the kinetics of the carbon oxidation. There is only about 200mV of overpotential on the cell, meaning that the cell is probably operating in the kinetically controlled region of the polarization curve, and should be minimally affected by any mass transport losses. In this specific analysis, the coal sample is analyzed for two reasons. First coal is abundant, and assuming that it can be properly cleaned prior to utilization, can be used as an excellent fuel supply. Second, since coal produced the third worst cell performance, if the rate of CO_2 production from this carbon source is enough to hinder the electrochemical reaction, then this case should have similar results for each of the other types of carbon fuels.

The sample of coal studied by Cherepy et al. (2005) was ground into particles ranging in diameter from 60nm to 10μm before being added to the molten carbonate electrolyte in the anode compartment. Following this, the cell was started and run through a polarization scan, from which the current density at 0.8V was reported. As previously stated, this is in the kinetically controlled region of the polarization scan, so the only reason for differences in performance would be changes to the fuel supply. At 65mA/cm^2, coal was one of the worst performers. However, this current density was based on the geometric surface area of the working electrode and independent of the electrochemical surface area, which would be a much more relevant quantity for studying the fundamentals. To gain a deeper understanding of the role that the coal surface plays in the production of CO_2, the reported current density from Cherepy et al. should be presented in based on the electrochemical surface area and not the geometric area of the working electrode.

A model is presented to determine the actual electrochemical surface area and real current density. This model assumes that each of the ground coal particles is a perfect sphere and all of the particles have a uniform diameter. The working electrode is assumed to be rectangular in shape with a length of l and a width of w. As shown in the figure below, the first layer of coal particles is laid on top of the current collector so that each of the particle's four neighbors has a single point of contact.

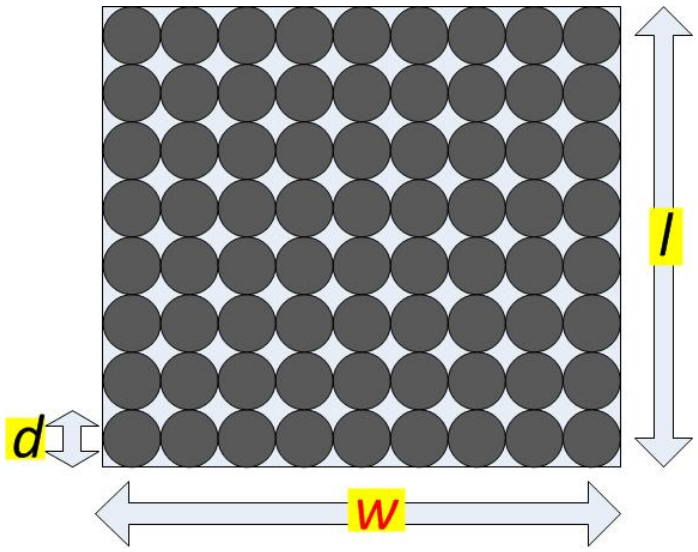

Figure 9: Geometric placement of the initial arrangement of coal particles in a DCFC

The shape of the electrode and particle distribution is most likely not an exact representation, but has several simplifying advantages. The arrangement and the total number of particles relies on simple mathematics as the total number of particles can be computed from the product of the number of particles in the horizontal and vertical directions, rather than a more complicated mathematical calculation.

The level of depth by which the reaction proceeds is an unknown. The work by Chen and Selman (2010) reports that carbon oxidation does not proceed past 40% of the length of the anode, however their model did not require electrical conductivity between the current collector and coal. The model presented here requires that the fuel have physical contact with the current collector because the electrical conductivity of the molten carbonate electrolyte (~1-3.5 S/cm; Kojima et al., 2008) is much lower than that of carbon (~100 to 10^4 S/cm; Pierson, 1993). While the electrolyte provides a certain degree of electrical conductivity, the easiest and most direct path for electrons to pass to the current collector is through direct contact between the carbon and nickel current collector.. Because it is easier for electrons to move via the carbon fuel, it model assumes

that direct connection between the current collector and carbon is required. This is plausible since as carbon is consumed, its radius decreases, thus allowing for the possibility of a loss in direct contact between adjoining layers, or at the very least, an increase in resistance due to the shrinkage of the electron conducting pathways. This may not necessarily be true, electrons may be able to pass from more than one layer, but initially, only one layer's surface area is assumed to be active.

The consumption of carbon and production of CO_2 is known to occur on the surface, and while the surface was assumed perfectly spherical for packing purposes, carbon (specifically the coal surface in this case) would not produce a smooth surface on any size scale. As was shown in the preceding sections, coal has a very porous structure, with a significant amount of impurities naturally found intertwined with the carbon. The composition is assumed to be pure carbon, such that any amount of impurities can be removed through one of several techniques that were described by Cooper (2004). To account for the porous nature of coal, and thus the rough surface, a "roughness correction" is applied to the surface area. Cherepy et al. (2005) and Botsaris (1989) both report that the specific surface area of coal is on the order of several hundred square meters per gram due to the internal porous structure, however not all the surface area will participate in the electrochemical reaction. Following the theory presented by Webb (1994), and shown in Figure 7, the molten electrolyte is not expected to penetrate the internal pore structure, and without the carbonate ion present, the electrochemical oxidation of carbon cannot be sustained in the interior pores. But since this porous network does leave the surface with craters and cavities, the "roughness correction" is used to account for any extra surface area that may be active. Applied to the surface of

each coal particle is a surface roughness of 200%, translating into a doubling of the predicted electrochemical surface area.

By using these assumptions, the model can be applied to predict the current density based on the electrochemical surface area and the production of CO_2 based on the surface area of active carbon (which is useful when performing numerical models of the gas growth). The true electrochemical surface area depends on the number and size of the individual particles that are present on the electrode. Beginning with the assumption that the electrode area has a rectangular shape, the area can be written as the product of the length and width of the electrode:

$$A = l \cdot w \tag{14}$$

For packing purposes, the particles were assumed to be perfectly spherical with a uniform diameter (d). The number of particles in the horizontal and vertical directions can be described as a function of their diameter and the width and length of the electrode, respectively. This is shown in the following equations:

$$N_h = \frac{w}{d} \tag{15}$$

$$N_v = \frac{l}{d} \tag{16}$$

The total number of coal particles can be determined by taking the product of the number of carbon particles in the horizontal and vertical directions.

$$N_{tot} = N_h \cdot N_v = \left(\frac{w}{d}\right) \cdot \left(\frac{l}{d}\right) \tag{17}$$

The numerator can be simplified by rewriting it in terms of the electrode area, which it the product of the length and width of a rectangle. This is the experimentally reported

electrode surface area, and thus a known value. The total number of particles now is only a function of the size of the particle.

$$N_{tot} = \frac{A}{d^2} \tag{18}$$

By approximating the surface of the coal as a sphere, the total electrochemical surface area can be written as the surface area of a sphere (with a uniform diameter of *d*) multiplied by the total number of particles. Also included is the "roughness correction" to better approximate the true active area.

$$ECSA = \zeta \cdot N_{tot} \cdot (\pi d^2) \tag{19}$$

By substituting Eq. 18 into Eq. 19, it is found that the electrochemical surface area is independent of the particle size, and a function of previously known values:

$$ECSA = \zeta \cdot \pi \cdot A \tag{20}$$

Several conclusions can be gathered from this result. First, the electrochemical surface area is larger than the reported electrode surface area by a constant factor. While it may be impossible to determine the actual surface area of the coal particles in the anode, the true electrochemical surface area is predicted to be much higher than the electrode geometrical area. Second, the size of the particle does not influence the reaction area. More numerous small particles (with a diameter of 60nm) would give the same amount of electrochemical surface area as fewer large particles (as would be the case with particles with a diameter of 10μm). This is an inherent result of the assumption that limits the electrochemical reaction to one layer of carbon particles.

Following from this analysis, a more accurate current density, based on the electrochemical surface area can be reported. First, the actual current, *I*, from the reported

current density and the electrode area needs to be recovered. This is done by applying the following equation:

$$j = \frac{I}{A} \tag{21}$$

Based on a 2.8cm^2 electrode, with 65mA/cm^2, the actual current that was recorded by Cherepy et al. (2005) was 182mA. By replacing the electrode area in the denominator of this equation with the more accurate active surface area of coal, the current density can now be based off of the electrochemical surface area, by replacing the geometric surface area with the electrochemical surface area from Eq. 20. By introducing this current density into Faraday's law, the amount of carbon consumed and CO_2 produced, based on the surface area of carbon, can be derived, as shown below. In this equation, the value '*n*' is dependent on the species of interest and relates the number of electrons that are produced per mole of said species. The constant of '*F*' is Faraday's constant

$$\dot{n}'' = \frac{j}{nF} \tag{22}$$

This version of Faraday's law is slightly different than the traditional representation in that it is based off of the current density and not the actual current. The resulting value, $\dot{n}''$, still produces the consumption and production rates of all reaction parties, but has units of [mol/s-cm^2], and a dependence on surface area. This is because when the current density is placed in the numerator, it adds information about the carbon surface, thus changing the result to a molar flux of consumption/production. The reason for this will be made clearer in part 4, where the mass flux, is used to determine the source term for the mass transfer. The mass flux can be found by multiplying the molar flux by the molecular weight of the corresponding species.

$$\dot{m}'' = M\dot{n}'' \tag{23}$$

By applying this model to the results obtained by Cherepy et al. (2005), the current density (based on the electrochemical surface area), consumption rate of carbon, and production rate of CO_2 can be determined. These are shown in Table 3.

Table 3: Estimated current density and consumption/production rates based on the surface area of carbon fuel from the work of Cherepy et al. (2005)

Current Density (mA/cm^2)	10.34
Consumption Rate of C ($mol/s\text{-}cm^2$ C)	2.68×10^{-8}
Production Rate of CO_2 ($mol/s\text{-}cm^2$ C)	8.04×10^{-8}

The results presented in the findings are odd when compared to the current densities achievable on platinum (Pt) in PEM fuel cells. If the PEM electrode is covered in 0.4mg Pt/cm^2, and operating at $1A/cm^2$, then the platinum itself is reducing oxygen at the rate of $5mA/cm^2$ Pt (assuming that 1g of Pt can have $50m^2$ of surface area). When comparing this to the result from Table 3, it seems that more than one layer of coal (possibly three or four) is active in the carbon oxidation. Since the kinetics of the carbon oxidation are sluggish, it is improbable that the carbon surface can have a higher activity than one of the best catalysts on the market. However without a methodology to track the electronic conductivity between the particles, it cannot be confirmed that multiple carbon layers are active.

Aside from the assumption of one layer of activity, the way that mass transport could be limiting would be due to the high rate of CO_2 production. For every carbon atom that are consumed on the surface, by Eq. 2, there are three CO_2 molecules that are produced, resulting in a high level of CO_2 initially in solution. In the work of Devyatkin et al. (2001), the reported solubility of CO_2 in a molten carbonate solution is only 10^{-4} mol/cm^3, while earlier work by Janz (1967) reported that the level of CO_2 soluble in

a molten carbonate solution is so low that it was immeasurable. Assuming that the 10^{-4} mol CO_2/cm^3 solubility level is accurate, that allows for only a small amount of CO_2 to be in solution before it evolves into gas bubbles. With the production rate of CO_2, and the continued accumulation in the electrolyte, this could lead to the formation of gas within the cell if not properly removed. According to Cooper (2004), continued development of DCFC's requires improved performance and a scaled up size, both of which would result in higher amounts of CO_2 production, which would need to be removed from the anode compartment, else the trapped CO_2 in solution could evolve out and form gas bubbles. This formation can be related to a fairly well studied phenomenon: that of nucleate boiling, which can provide an analogy for this cell's operation.

3.3 Hydrophobic Boiling Process & Analogy to CO_2 Bubble Growth

To understand the physics of CO_2 bubble formation and growth in the anode of a DCFC, a proper analogy would be to compare this process with that of boiling, another physical process that studies the formation, growth, and departure of vapor bubbles in a liquid. While the two mechanisms that initiate the processes are different, the growth and departure of the bubbles obey the same physics. Inside the DCFC, CO_2 gas will evolve when the concentration of CO_2 in the molten electrolyte in solution exceeds the solubility level ($\approx 10^{-4}$ mol/cm^3). Boiling occurs when a liquid is superheated, that is its temperature exceeds the saturation temperature, so the liquid begins to vaporize (Faghri, 2006).

Boiling is a process that begins when a liquid is heated to a temperature above its saturation temperature at a given pressure. The liquid begins to form vapor bubbles through one of two processes: either heterogeneous or homogeneous boiling, which

require different starting mechanisms (Faghri, 2006). Homogeneous boiling occurs within the liquid continuum when it is superheated to a temperature significantly higher than the saturation temperature, where vapor bubbles begin to form randomly within this phase. Heterogeneous nucleation requires a lower level of super-saturation, but also an interface with a heated surface. As the liquid, e.g. water, is heated at the surface, small bubbles are formed at nucleation sites on the surface. Once a bubble has been formed, the forces acting on it are nearly identical, resulting in the bubbles eventually departing the surface and traveling through the liquid until it reaches the surface due to buoyant forces (Faghri, 2006). In recent years, this theory has been changed by analyzing the surface properties that affect boiling, surface properties that may influence the CO_2 bubble growth on the carbon surface.

Earlier in this section, the process by which CO_2 gas was formed was described: exceeding the saturation concentration, which is already not very high. Boiling was a process that involved much of the same physics, and was shown to have two different mechanisms. This CO_2 gas is known to exist in the electrolyte solution, which must have been transferred through a process similar to boiling. If that is the case, then the formation of CO_2 gas can occur in two similar mechanisms, with a preferred mechanism. This gas is assumed to exit the anode through an air tight seal at the top of the cell (Cherepy et al., 2005). Chen and Selman (2010) have produced a 1D model which attempts to predict the current and concentration profiles. While neglecting the formation mechanism of the gas bubbles, the model does account for gas bubbles present in the anode. Presumably these bubbles would be formed homogeneously; however the alternative bubble growth approach was not examined. This would not explain the visible

craters on the graphite sample shown in Figure 8. To study the formation of these craters, an examination of the carbon surface and nucleation sites is presented.

Hong and Selman (2004) were the first the report that the wettability of the carbon may be an important factor. Chen et al. (2012) also proposed this theory through their experimental work with several different carbon based fuels. They found that by either adding electrolyte to the anode, or premixing the electrolyte-carbon source first, they could improve laboratory scale test results, and concluded that the wetting of carbon by the electrolyte allows for better access of the carbonate ion to the surface. While it is an important result, the non-wetting tendency has further amplifications than just allowing for each of the reactants to be available to the carbon surface. For any defect on the surface of the carbon, the electrolyte must pass over this region as the particle is immersed in the solution. The process, as described by Webb (1994) and presented in §*3.1 Problem Statement*, does not cover the entire surface with electrolyte. As shown in Figure 7, when the electrolyte gets in contact with the solid fuel surface, gas becomes trapped in surface cavities. Since as much as 50% of the volume of a coal particle may be void space occupied by gas, there would be many imperfections that would be suitable for trapping gas within this area (Botsaris, 1989). This gas pocket can then act as a nucleation site for CO_2 bubble formation, in much the same way that trapped gas pocket can facilitate the onset of heterogeneous boiling. It is not proposed that this process occurs at the moment of startup, but this is an issue that can amass through continued use after only a few minutes.

The primary physics of classical heterogeneous boiling, also called pool boiling, can be broken down into four distinct heat transfer patterns. Figure 10 displays the four

regions which are described by Faghri and Zhang (2006), and have been proposed to be true for all surfaces in which vapor bubbles are assumed to be able to depart the surface.

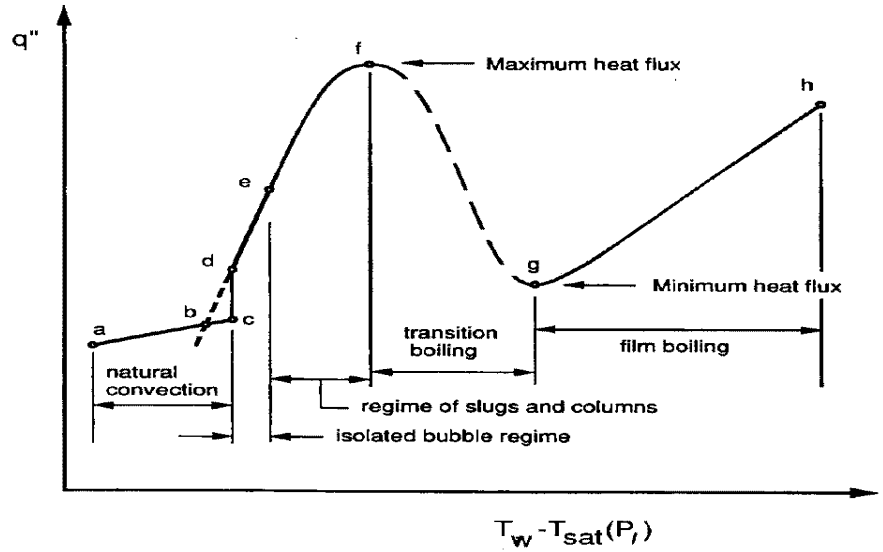

Figure 10: Heterogeneous boiling curve displaying the four regions in which heat is transferred to the fluid (me.umn.edu)

The first region occurs at low levels of super-saturation, where the temperature of the surface (T_w) is slightly above the saturation temperature (roughly from points a to c). At this point, only heat transfer occurs without phase change. As the liquid is further heated (from points d to f), vapor bubbles begin to form in a process called nucleate boiling. This is the critical process which begins the process of vapor formation to increase the rate of heat transfer. At a specific level of super-saturation, the fluid is expected to reach a maximum heat flux, also called the critical heat flux (point f), at which point, further increases in temperature result in a drop in heat transfer through what is called transition boiling. The rapid formation of vapor bubbles that began from the onset of nucleate boiling begins to become unstable, and forms an unstable vapor film between the surface and the liquid. Eventually, a minimum heat flux is reached (at point g), where the entire surface is covered in a relatively stable vapor film, and further heating of the surface

results in an increased heat transfer through the vapor film and into the liquid. This had been the classical theory published in many textbooks; however, recent studies about the effect of surface wettability have shown this theory to be incomplete.

The first account issued about the heat flux in nucleate boiling was reported in the work of Rohsenow (1952). Through his research, he was able to correlate the level of super-saturation, to the predicted heat flux through the Eq. 24, known as Rohsenow's pool boiling correlation. The mass transfer, from liquid to vapor phase, could then be predicted by applying the latent heat of vaporization in Eq. 25.

$$q" = \mu_l h_{lv} \left[\frac{g(\rho_l - \rho_v)}{\sigma}\right]^{1/2} \left[\frac{C_{p,l}(T_w - T_{sat})}{C_{s,f} h_{lv} Pr_l^n}\right]^3 \quad (24)$$

$$q" = h_{lv} m" \quad (25)$$

In Eq. 24, two variables are introduced to model the effect of the fluid and the heated surface ($C_{s,f}$ and n). Pioro (1999) studied the heat transfer rate in several different combinations of fluids and surfaces, and found that there is almost a unique combination of values for each different fluid and surface combination. As can be seen in many different textbooks (Faghri and Zhang, 2006; Incropera et al., 2007), this powerful relationship is frequently promoted as the best correlation for predicting heat and mass transfer in a nucleate boiling regime, however, this correlation has also been the target of criticism. Fand and Ho (1977) have published literature questioning the validity of Rohsenow's correlation. In their paper, Fand and Ho describe experimental situations where the data does not match up with Rohsenow's prediction. Their disagreements are based in the determination of the constants ($C_{s,f}$ and n). First, according to their analysis, the parameter concerning the surface finish ($C_{s,f}$) should have a dependence on the applied heat flux and pressure. They also disagree that the exponent on the Prandtl

number (n) can vary in magnitude. This comes from traditional dimensional analysis, in which the exponent on a dimensionless number should be fixed. Thus they assert that this value should be constant for any fluid, and not variable as Pioro, (1999) has shown. While Fand and Ho have described a couple of disagreements with Rohsenow's analysis, there is a larger issue that Rohsenow and others did not consider, the wettability of the surface by the liquid. In more recent literature, the effect of the contact angle and surface tension were more accurately portrayed, and provide a better description of the bubble tendencies in a DCFC.

More recent literature about nucleate boiling has studied the relationship between the fluid and surface, specifically, the effects that the contact angle has on the heat transfer. The recent works of Phan et al. (2009) and Takata et al. (2010) have showed that the heterogeneous boiling process is far more complicated when the wetting tendencies are included in the analysis. Both of these papers describe experiments in which non-wetting fluids (with a contact angle greater than 90°) produce a boiling process which does not follow the theory of classical heterogeneous boiling, as shown in Figure 10. This work is critical since it changes the fundamental understanding of boiling heat and mass transfer.

The theory of Rohsenow (1952) was based on the assumption that the surface was wetting, and that the bubbles would eventually depart once the buoyant force exceeded the surface tension force. When that is not the case, this analysis breaks down, as larger bubbles must be formed to produce enough lift to depart the surface. The work of Phan et al. (2009) describes this phenomena by testing both hydrophilic (wetting, $\theta < 90°$) and hydrophobic (non-wetting, $\theta > 90°$) surfaces. Beginning with a solid stainless steel base,

this group coated the surface with different materials to produce contact angles ranging from 20° to 110°, in an attempt to better describe the boiling process's dependence on the wettability. It was assumed that these surface finishes did not alter the topology.

For hydrophilic surfaces, Phan et al. (2009) described the standard boiling process, with bubbles forming, growing, and departing form the surface. The process would then repeat, however, an interesting trend was observed. As the contact angle was lowered, the size of the bubble at departure increased, thus resulting in a decreased bubble detachment frequency. This they claim to be in contrast with previous literature.

The most important work from Phan et al. (2009) came from studying the nucleation and growth of bubbles form a hydrophobic surface. Two cases were considered, with contact angles of 104° and 112°. In both cases, the exact same physics was observed; bubble nucleation and growth proceeded according to traditional theory, but with different results. The fluid was only slightly supersaturated at the onset of boiling (the exact level of super-saturation was not given). However, the critical observance was that no bubbles detached. Rather, due to the surface tension force and the contact angle, these bubbles spread on the surface, eventually merging to bring an onset to film boiling. This was accomplished by not departing any vapor bubbles and without reaching the predicted critical heat flux. Images of these surfaces are shown in Figure 11.

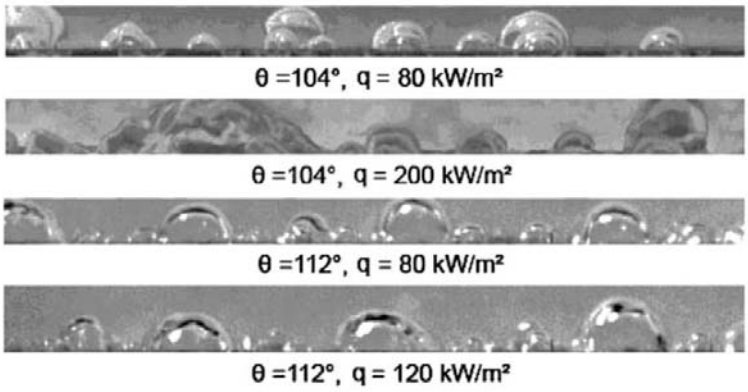

Figure 11: Nucleate boiling on non-wetting surfaces depicting inability to depart and transition to film boiling. Images by Phan et al. 2009

A similar experiment was conducted by Takata et al. (2010) and described the same physics. In several different cases, this group modified the surface to even more hydrophobic surfaces than did Phan et al. (2009). Takata et al. (2010) studied surfaces with contact angles of 127° and 150°, and produced more detail about the process. Hydrophilic surfaces were described as requiring at least 10°C of super-saturation to begin the boiling process, while hydrophobic surfaces required at most 3°C of super-saturation to begin bubble growth. With a contact angle of 150°, the level of super-saturation required at the onset of boiling could not be recorded because it was too low to measure. Again, on a smooth surface, as the bubbles grew, they spread on the surface. These did not detach, and caused an early start to film boiling. Upon lowering the temperature this film boiling was observed to remain until 90°C (10°C below the atmospheric boiling temperature). There was no explanation provided for this effect. Different than Phan et.al, they were able to induce bubble departure on hydrophobic surfaces by varying the surface composition. Takata et al. had spotted a hydrophilic surface with hydrophobic areas. Since nucleation starts at lower levels of super-

saturation, bubbles form on these hydrophobic surfaces first. These bubbles grow until they reach the edges of hydrophobic surface where, at the interface, the bubbles detach.

From these two works, it is concluded that bubble growth and departure is heavily dependent on the ability of a fluid to wet the surface. Non-wetting surfaces are favorable locations for the onset of nucleate boiling, and do not allow for the detachment of vapor bubbles prior to the start of film boiling. Carbon dioxide generation in a DCFC anode is generated by an electrochemical reaction rather than phase change, but the nucleation and growth of CO_2 bubble in a DCFC resembles the growth of a bubble in a nucleate boiling process. If this is true, the elements are in place to describe the growth of CO_2 in the surface of the carbon with the same physics that are used to model a boiling mechanism. Since the carbon surface is imperfect, consisting of defects and surface roughness, there exist cavities for initial gas entrapment, and because carbon is non-wetting, it is reasonable to predict that the growth of CO_2 gas is similar to boiling on a non-wetting surface. Combining these factors, the growth of gas on the surface would, in theory, cover the carbon particles, thus reducing the available surface area, and stopping the electrochemical reaction due to loss of contact of the solid surface (carbon) with the carbonate ion. To do this, it must be proved that for a non-wetting surface, the departure size of a gas bubble exceeds the available area of the carbon particle, and that this process can occur before it is consumed in the electrochemical reaction.

3.4 CO_2 Gas Departure within a DCFC

When a gas bubble grows on any surface (whether is a water vapor bubble in a boiling process, or a CO_2 gas bubble on a carbon particle), the force balance incorporates the same forces. As growth occurs, five forces act either to keep it attached to the surface or to detach it. Faghri and Zhang (2006) refer to these five forces as products of inertia, drag, buoyancy, surface tension, and gas pressure. Inertia forces are caused by mass transfer to the bubble, and depend on the rate of change of the bubble radii. The growth of the bubble causes the surrounding liquid to move, resulting in a velocity field that induces the drag force. In the case of a static bubble, there is no growth or induced velocity field, thus negating the effect of these terms. Faghri and Zhang also consider that the internal pressure in a bubble influences its motion since this pressure higher than the pressure of the surrounding fluid. This force would act as a net force that works to detach the bubble; however, this force produces no net x directional force, and has little to no influence when compared to the buoyant and surface tension forces, and thus can be neglected.

While static bubbles do not consider the effect of external motion outside the bubble, these types of bubbles allow for a quick estimation of the bubble's departure size. Static gas bubbles are heavily dependent on the force balance between surface tension and buoyancy forces. These forces oppose each other as the surface tension acts along the edge of the bubble to keep it attached to the surface. In a two dimensional plane, the forces acting parallel to a horizontal surface combine to produce zero net force, though the component that acts vertical to the surface must be considered. This force is dependent on the length of the base of the bubble, the surface tension coefficient, and the

contact angle, which combine to define its shape. This relationship is shown in the following equation, where the sine of the contact angle constitutes the vertical component of the surface tension force. For a circular base, the length can be replaced with the circumference of the bubble's base radii.

$$F_\sigma = l\sigma \sin\theta \tag{26}$$

The opposing force that acts against this surface tension force is the buoyant force. When applied to growing gas bubbles, buoyancy acts to detach the bubble from the surface because the density of the liquid is greater than the gas. While the weight of the bubble opposes this lift force, the net buoyant force can be calculated from the following equation.

$$F_{buoy} = (\rho_l - \rho_v)gV \tag{27}$$

When the buoyancy force is sufficient to counter the surface tension, further mass transfer into the bubble (i.e. bubble growth) will initiate departure from the surface. This is shown in the following two relationships.

$$F_{buoy} = F_\sigma \tag{28}$$

$$(\rho_l - \rho_v)gV = \sigma(\pi d_b)\sin\theta \tag{29}$$

Classical application of this relationship had been accomplished by assuming that the volume of the gas bubble was spherical in shape, and that the base diameter was either known or could be calculated. This is a reasonable approximation for wetting surfaces where to contact angle is less than 90°. But there is no real application done to this equation for non-wetting surfaces. As Phan et al. (2009) and Takata et al. (2010) have shown that bubble detachment from hydrophobic surfaces is not known to happen prior to the start of film boiling.

To determine the size and shape of the gas bubble at departure, its geometry needs to be resolved. Since Faghri and Zhang (2006) had assumed that the nucleation process occurs on a hydrophilic surface, the volume of the bubble has been approximated by a sphere. This idea has been reproduced in several works including Incropera's heat transfer textbook (2007), and a review of nucleation fundamentals by Jones et al. (1999). But, for non-wetting surfaces, the bubble does not grow in a spherical shape, but in the shape of a spherical cap. For DCFC applications, carbon is known to be a non-wetting surface, so a more realistic application of the departure size and shape would apply this spherical cap geometry. By applying this model to the CO_2 gas on a carbon surface, it can be shown that size of a departing bubble exceeds the size of the particle, and that the surface area covered would equate to a loss in electrochemical surface area that translates into lower performance. The volume that Faghri and Zhang presented is distinctly different as displayed in the spheres in Figure 12, showing the difference in shape for bubbles growing on wetting and non-wetting surfaces.

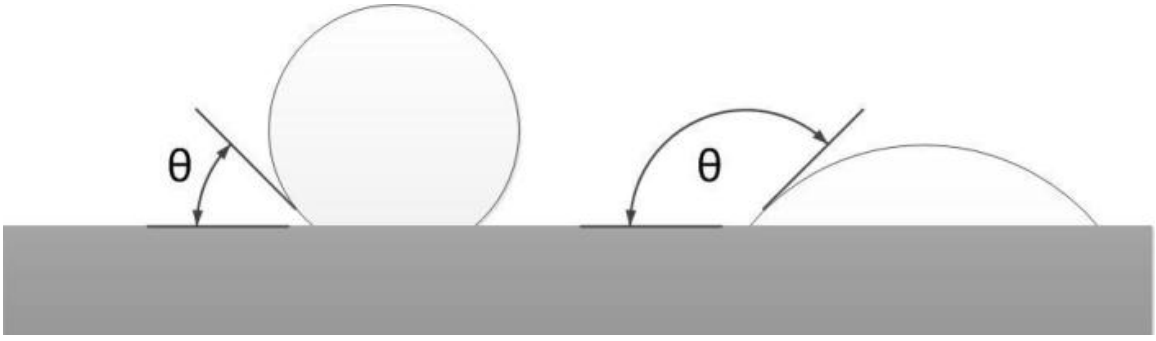

Figure 12: Bubble shape when placed on a wetting surface (left) and a non-wetting surface (right)

Immediately, it is noted that the difference in shape requires a different definition of the bubble volume. By approximating the shape of the bubble as a spherical cap, the volume for this cap is determined in the following fashion.

$$V_{cap} = \frac{\pi}{3} h^2 (3R - h) \tag{30}$$

In this equation, 'h' is the maximum vertical distance between the surface and the cap, and 'R' represents the radius of a sphere through which the cap was created.

By utilizing the true volume of a gas bubble, it is proposed that for every contact angle, there exists a unique volume for departure which can be mathematically supported by solving Eq. 28, in conjunction with the true geometric shape of the bubble. To accomplish this, a relationship between the diameter of the base (which is a minor chord within a circle) and the volume of a sphere should be formulated. This is done through a geometric proof that is found in *Appendix B: Supplemental Mathematics for Gas Bubble Departure*. Through geometric analysis, it is shown that in a three dimensional geometry, there is a one-to-one correspondence between the contact angle and the size of a spherical cap that is produced. This means that for all surfaces, including non-wetting surfaces ($90° < \theta < 180°$), there is a single volume that represents the balance of surface tension and buoyant forces. For non-wetting surfaces this volume can be represented as a spherical cap whose volume is given by Eq. 30. The relationships between the bubble size and the parameters 'R' and 'h' are shown in the following two relationships, available in *Appendix B*.

$$R = \frac{d_b}{2} \csc\theta \tag{31}$$

$$h = \frac{d_b}{2} (\csc\theta - \cot\theta) \tag{32}$$

With the geometry resolved, the predicted bubble detachment size can be computed. There are three distinct cases that can be solved with a simple force balance from a free body diagram. These cases include wetting, non-wetting, and neutral surfaces,

depending on the contact angle. Wetting surfaces ($0° < \theta < 90°$) will tend to bead the bubble, causing the shape to look like the bubble on the left of Figure 12. This volume can be approximated as a sphere less a spherical cap whose volume is dependent on the contact angle. For a neutral surface ($\theta = 90°$), the bubble should contract into the shape of a hemisphere. On a non-wetting surface ($90° < \theta < 180°$), the gas bubble would form only a spherical cap, whose volume can be represented by Eq. 30. By performing the force balance, the size of the gas bubble upon departure will be derived for a non-wetting surface.

To set up the governing physics, a free body diagram is created showing the buoyant and surface tension forces acting on a gas bubble.

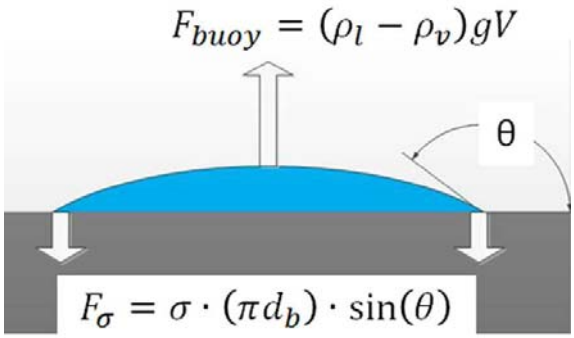

Figure 13: Free body diagram of a static gas bubble on a non-wetting surface

By equating the two forces, Eq. 29 can be reproduced.

$$(\rho_l - \rho_v)Vg = \sigma(\pi d_b)\sin\theta \tag{29}$$

To solve this equation, as a function of the contact angle only, Eq. 29 should be rewritten, with the base diameter a function of the fluid properties, contact angle, and total bubble volume. This is represented in Eq. 33.

$$d_b = \frac{(\rho_l - \rho_v)gV}{\sigma\pi}\csc\theta \tag{33}$$

This form of the equation leaves two unknowns, the base diameter and bubble volume. Since the surface is non-wetting, the volume of the gas bubble is equivalent to the volume of the spherical cap.

$$V = V_{cap} \tag{34}$$

$$V = \frac{1}{3}\pi h^2(3R - h) \tag{35}$$

By use of the geometric proof the quantities 'R' and 'h' are known through Equations 31 and 32. By substituting these relationships, the volume can be written as a function of the contact angle and base diameter. This is shown in Eq. 36, and simplified in Eq. 37.

$$V = \frac{\pi}{3}\left(\frac{d_b}{2}\right)^2 (\csc\theta_s - \cot\theta_s)^2 \left[3\left(\left(\frac{d_b}{2}\csc\theta_s\right) - (2\csc\theta_s - \cot\theta_s)\right)\right] \tag{36}$$

$$V = \frac{\pi}{3}\left(\frac{d_b}{2}\right)^3 (\csc\theta_s - \cot\theta_s)^2(2\csc\theta_s + \cot\theta_s) \tag{37}$$

Note the use of θ_s in the previous equations. It is defined as the supplementary angle to the contact angle, and is used based on the definition of the contact angle being the angle between the surface and the gas, that is: the angle outside the gas bubble (shown in Figure 13). By substituting the volume into force balance (Eq. 33), the base diameter can be calculated for a gas bubble on the verge of departure.

$$d_b = \left(\frac{(\rho_l - \rho_v)g}{\sigma\pi}\csc\theta\right)\left(\frac{\pi}{3}\right)\left(\frac{d_b}{2}\right)^3 (\csc\theta_s - \cot\theta_s)^2(2\csc\theta_s + \cot\theta_s) \tag{38}$$

After rearranging, the diameter of the base can be calculated by use of the following equation:

$$d_b^2 = \frac{24\sigma\sin\theta}{g(\rho_l - \rho_v)}[(\csc\theta_s - \cot\theta_s)^2(2\csc\theta_s + \cot\theta_s)]^{-1} \tag{39}$$

From this equation, a single base diameter can be calculated from a known contact angle. This can then be inserted into Eq. 35 to determine the volume that the gas would need to displace in order to depart the surface. Note that Equations 33 through 39 apply only to non-wetting surfaces, and that a different geometry will need to be applied to determine the exact size and shape of the departing gas bubble.

Applying the required geometry allows produces different estimates of the bubble departure size. For the wetting and neutral surfaces, a complete solution to the force balance is found in *Appendix B*. The results from these two cases are shown here in the following three functions. For a wetting surface, the when the force balance is applied to a correct geometry, the volume would be written as the volume of a sphere less the volume of a spherical cap (whose size depends on the contact angle):

$$V = \frac{4}{3}\pi R^3 - \frac{1}{3}\pi h^2(3R - h) \tag{40}$$

And the corresponding base diameter at departure would be:

$$d_b^2 = \frac{24\sigma \sin\theta}{g(\rho_l - \rho_v)}[4csc^3\theta - (\csc\theta - \cot\theta)^2(2\csc\theta + \cot\theta)]^{-1} \tag{41}$$

In the case of a neutral surface, the volume would be equal to half of a sphere, and the base diameter could be written with the following equation. This could also be reproduced by solving Eq. 41, the base diameter for a wetting surface, with a contact angle of 90°.

$$d_b^2 = \frac{12\sigma}{g(\rho_l - \rho_v)} \tag{42}$$

In each of the three cases, the bubble departure size has been shown to be dependent on the contact angle, with a unique solution. To solve for the correct base diameter and volume at departure, the proper fluid properties must be used in each of the

relationships. These molten carbonate electrolyte properties were obtained primarily from the work of Janz et al. (1961, 1963). In this work, selected fluid properties of the individual electrolyte components (Li_2CO_3, Na_2CO_3, K_2CO_3), along with selected mixtures, were published. Unfortunately, the work was not consistent for three main reasons. First, the temperature ranges at which the properties are given are different for each component, resulting in the inability obtain mixture quantities thermodynamically. This is further complicated by the fact that when the three components are mixed, their melting point is lower than it would be for the individual constitutes. Since Janz et al. have presented some mixture property data, a rough estimate of the fluid properties could be approximated, but this produces further problems. Each of the papers used different electrolyte mixtures, including one with containing no lithium carbonate. This is a problem since lithium carbonate is added to the electrolyte to reduce its melting point and help facilitate the production of the carbonate ion at the cathode, thus it cannot be left out. This results in an incomplete knowledge of the fluid properties. The actual measured property values for the individual carbonates compounds are shown in *Appendix A*. From these results the best approximation of the electrolyte density (ρ_l) and surface tension (σ) are shown in Table 4 for a mixture of equal parts Li_2CO_3-Na_2CO_3-K_2CO_3.

Table 4: Fluid properties of the molten electrolyte for calculation of the force balance

Density (ρ_l)	1900 kg/m^3
Surface Tension (σ)	0.2 N/m

The density of carbon dioxide can be derived from the ideal gas law:

$$P = \rho RT \tag{43}$$

For a DCFC operating at 750°C with atmospheric pressure, the density of CO_2 is roughly 0.5242kg/m^3, or 3600 times smaller than the density of the electrolyte mixture. Because

the buoyant force relies on the density difference, the CO_2 gas density has a minimal effect on the force balance, and thus can be neglected. The bubble departure size can now be calculated.

Based on the geometry of the bubble, the correct shape and size were determined through the presented analysis, but perhaps more importantly, the area covered by this bubble can be calculated. If a circular surface area is assumed, then the covered surface area would be a function of the base diameter (as calculated in Equations 39, 41 and 42).

$$A_c = \frac{\pi d_b^2}{4} \tag{43}$$

This is important to show how much of the surface is covered during bubble growth. The work of Phan et al. (2009) and Takata et al. (2010) have shown that, on non-wetting surfaces, this spreading tendency causes water vapor bubbles to merge and begin film boiling. A similar phenomenon may occur on the surface of carbon, but more importantly, the amount of surface area covered results in a loss of electrochemical surface area. Without access to the carbonate ion, which would be blocked by the CO_2 gas film, the coal becomes useless. To see this effect, the results of this analysis are shown in Figure 14:

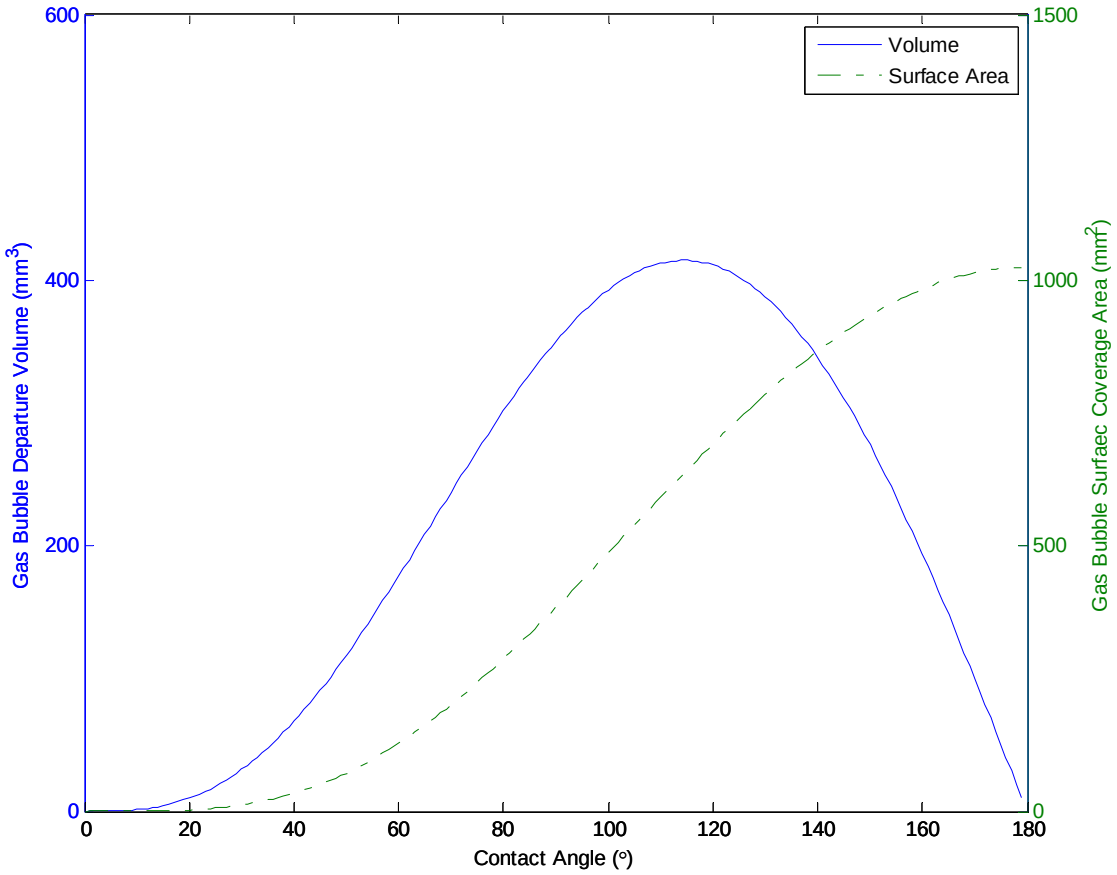

Figure 14: The predicted bubble departure volume (-) and covered surface area (- - -) for CO2 bubbles formed on the surface of carbon.

The results of this study show increasingly large surface area coverage for non-wetting and slightly wetting surfaces. The theory for bubble formation was established in §*3.3 Hydrophobic Boiling Process & Analogy to CO_2 Bubble Growth* and based on this analysis, the departure bubble size was forecast through a force balance that resulted in the predicted the CO_2 bubble departure information on the surface of the coal. If the CO_2 bubble formed on a wetting surface, the theory predicts that the bubble departure volume and surface area coverage both increase with increasing contact angle. While this is in opposition to the observations of Phan et al. (2009) who saw larger vapor bubble volumes at departure as the contact angle heads towards zero degrees, for hydrophobic cases, it

agrees that bubble departure size is significant to cover the surface. The effects of inertia and drag may influence the departure volume at these levels; however, the results still indicate that gas bubbles should be able to depart from wetting surfaces. As the contact angle increases, the physics indicates that the bubble volume and covered surface area also increase, to extremely large sizes. The required surface area (dashed line) shows that not only the merging of multiple bubbles could occur, but single vapor pockets could expand to produce large base diameters that produce a vapor film similar to that observed in boiling on a hydrophilic surface.

As the surface transitions from a wetting surface to a non-wetting one, the geometry and related mathematics produce changes to the bubble departure volume and surface area. Because the contact angle makes the bubble form a spherical cap on a non-wetting surface, the volume reaches a maximum when the contact angle is 114°, while the surface area covered by the vapor cap continually expands. The height of said cap decreases as the contact angle increases, thus resulting in a drop in bubble volume, while the base diameter continues to increase. Thus, the more non-wetting the surface, the larger the predicted surface area coverage would be, but also the thinner the bubble. This extremely thin film may have the potential to be unstable, but even when considering less non-wetting surfaces, with contact angles closer to 90°; the covered area is still significant. In the laboratory, the largest carbon particle that has been introduced to the DCFC anode was reported by Li et al. (2010a) as being a coal sample 2mm in diameter. If the surface is slightly wetting (≈100°), as has been predicted by Hong and Selman (2004) and Chen et al. (2012), then the surface area required to achieve detachment for one bubble would be nearly 33 times larger than the area of the coal particle used. It is

reasonable to assume also that more than one gas pocket would exist on that surface of the coal that would be capable of producing CO_2 bubbles. The growth of several bubbles would spread along the surface, in a fashion similar to that has was shown by Phan et al. (2009) and Takata et al. (2010) in their hydrophobic boiling experiments. The eventual merging of these bubbles would cut off access to the molten electrolyte, by forming a vapor film over at least part, if not all, of the carbon particle surface.

The loss of electrochemical surface area would be a significant factor in the drop in performance that is visible in DCFC's. Referring back to the work of Li et al. (2010a), their use of coal produced current densities (based on the geometric electrode area), that were a third of the value that Cherepy et al (2005) were able to reproduce. Other than the source of their coal (Queensland Australia versus Kentucky U.S.A.), the primary difference was in particle size (1-2mm versus 60nm-10μm).While this suggests that smaller particles may be less affected by the proposed CO_2 coverage, it does not rule out the possibility that this phenomena does not occur on smaller particles. Returning to Figure 8, after the graphite sample was removed from its electrolyte bath, there were significant cavities formed by gas pockets on the surface. For larger samples, the formation of gas bubbles on the surface of the carbon fuel does have a level of influence on the poor performance seen in the oxidation of carbon, but for smaller carbon particles immersed in the anode, the same issue is present. In order to prove the existence of these mass transfer limitations, from large to small scale, the implementation of computational fluid dynamics (CFD) is used to show the gas growth on the surface of the carbon.

3.5 Coal Consumption Timescale

In the previous two sections, a theory for gas bubble formation and bubble departure has been proposed. This occurs on the carbon surface due to the imperfections that can trap small gas pockets on the carbon surface, which facilitate the bubble formation. For this predicted phenomena to have any influence on the performance of a DCFC, it is important to understand the time it takes for a bubble to grow relative to the time it takes to consume the carbon. The electrochemical surface area has been shown to be independent of the initial particle size by Eq. 20. The only remaining factor that original particle size influences is the carbon lifetime in the anode. Whether small or large particles are present in the oxidation reaction, the reaction rate would consume the carbon fuel at identical rates. Larger particles in this case would last longer than smaller particles, thus resulting in a longer period for the gas bubbles to grow. That growth can in turn result in gas bubbles of sufficient size that could limit the electrochemical surface area. Thus the time it takes to consume an entire particle now becomes of interest.

Continuous use of the DCFC has been shown to result in a buildup of carbon dioxide in the electrolyte solution, eventually reaching the saturation concentration. Exceeding this saturation level, results in the onset of bubble formation has had been described in previous sections. To study the lifecycle of a carbon particle, there are several assumptions that are required. Many of the same assumptions were previously defined in §*3.2 Determination of the Electrochemical Surface Area and CO_2 Evolution Rate.* Among the assumptions used to simplify the mathematics, the particles are assumed to be pure carbon, and have a perfectly spherical geometry whose area and volume are functions of time:

$$A(t) = 4\pi(R(t))^2 \tag{44}$$

$$V(t) = \frac{4}{3}\pi(R(t))^3 \tag{45}$$

For a complete description of the lifecycle, the radius of the particle, as a function of time, must be known. It is further assumed that the reaction occurs uniformly on the surface, causing the radius to decrease at a constant rate throughout the consumption process. This results in the individual particles retaining their spherical shape throughout the process. If the bubble formation predicted in the previous sections occurs, then this assumption would be invalid since gas would cover part of the surface, reducing its electrochemical surface area from what is predicted in Eq. 44. To start this analysis, the density of the carbon source is utilized to relate the mass consumption rate to the volumetric rate of change as shown below.

$$\dot{m} = \rho\dot{V} \tag{46}$$

Where the time derivative of the carbon volume can be obtained by use of the Chain Rule

$$\dot{V} = \frac{dV}{dt} = 4\pi(R(t))^2\frac{dR}{dt} \tag{47}$$

This analysis introduces a variable, the rate of change of the particle radii (*dR/dt*), which would contain information about the particle size. By combining the volumetric rate of change with the mass consumption rate, the radial rate of change can be determined. To calculate this, the total mass consumption rate ($\dot{m}$) would need to be rewritten as a function of the radius. This can be done through use of the following formula, relating the area specific rate of carbon consumption to the carbon surface area as a function of time:

$$\dot{m} = \dot{m}'' \cdot A(t) \tag{48}$$

The mass consumption flux ($\dot{m}''$) describes the amount of carbon consumed per unit area of carbon surface, and was described in Equations 22 and 23. Thus the total mass transfer rate is simply this flux multiplied by the existing surface area. The area is shown in Eq. 44 and when combined with Eq. 47 for the volumetric rate of change, and introduced into Eq. 46, then the rate of change of the particle radius can be determined.

$$\dot{m}'' \cdot A(t) = \rho\left(4\pi(R(t))^2 \frac{dR}{dt}\right) \tag{49}$$

$$\dot{m}'' \cdot 4\pi(r(t))^2 = \rho\left(4\pi(R(t))^2 \frac{dR}{dt}\right) \tag{50}$$

$$\dot{m}'' = \rho \frac{dR}{dt} \tag{51}$$

This shows that, based on the required assumptions, the carbon fuel particles decrease at a constant rate proportional to the current drawn and the carbon density. By integrating this equation, the particle radius as a function of time can be found by integrating the function.

$$\frac{dR}{dt} = \frac{\dot{m}''}{\rho} \tag{52}$$

$$dR = \frac{\dot{m}''}{\rho} dt \tag{53}$$

$$\int dR = \int \frac{\dot{m}''}{\rho} dt \tag{54}$$

$$R(t) = \left(\frac{\dot{m}''}{\rho}\right) t + C \tag{55}$$

In this equation, the constant (C) can be found by the initial condition, which would be the initial particle size.

$$R(t) = R_o - \frac{\dot{m}''}{\rho} t \tag{56}$$

This is consistent with the idea that the electrochemical reaction occurs uniformly around the carbon surface, resulting in the radius decreasing at a constant rate. Because the carbon is consumed, the mass flux is a negative term, which results in a decreasing radius. The mass flux can be recalculated to determine the consumption rate at any current density. This equation is only valid for the times where particle exists:

$$t < \frac{r_o \rho}{\dot{m}''} \tag{57}$$

From this equation, the lifetime of the particle can be measured, and compared to the time required for a CO_2 gas bubble to grow. This timescale will be used in the following sections to compare the growth rate of gas in a saturated electrolyte, to the consumption time of the particle. This would show whether the bubble growth can occur on the carbon surface prior to the carbon being consumed.

The last step to determine the longevity of the particles in solution is to input the proper property values into the equations. The mass consumption flux of carbon (specifically coal derived carbon) is obtained from the work of Cherepy et al. (2005), as was calculated in §*3.2 Determination of the Electrochemical Surface Area and CO_2 evolution Rate*. At an operating potential of 0.8V, the rate of carbon consumption was 2.68×10^{-8}mol/s-cm^2 (3.216×10^{-7}g/s-cm^2), and particles ranged in size from 60nm to 10μm. Cooper (2004) has written that most coal densities range from 0.8-1.2 g/cm^3, so densities of 0.8, 1.0, and 1.2 g/cm^3 will be examined. The lifecycle of the carbon source is shown in Table 5.

Table 5: Time to consume a coal particle in a DCFC anode operating at 10.34mA/cm^2

Initial diameter	Density	Lifetime
1mm	0.8 g/cm^3	34hrs
	1.0 g/cm^3	43hrs
	1.2 g/cm^3	52hrs
10μm	0.8 g/cm^3	21min
	1.0 g/cm^3	26min
	1.2 g/cm^3	31min
1μm	0.8 g/cm^3	2min
	1.0 g/cm^3	2.5min
	1.2 g/cm^3	3min
60nm	0.8 g/cm^3	7sec
	1.0 g/cm^3	9sec
	1.2 g/cm^3	11sec

This table shows that a significant amount of time is required to consume a coal particle in the kinetically controlled region of the polarization curve. If more current was drawn (the most achievable with a coal fuel source was reported by Cooper, 2004, as 300mA/cm^2) then the times required to consume the entire coal particle would drop by roughly 78% but would still require a significant time to consume relatively large particles (≈30sec for $R_o \geq 1\mu m$). With this being the case, there may be sufficient time for CO_2 to saturate the electrolyte, and produce gas bubbles that form, grow, and cover the carbon surface.

This analysis is not intended to capture the exact consumption physics or timescales. There are several assumptions which may lead to the carbon being consumed faster, including the impurities associated with carbon source, the void spaces and surface imperfections, and the fact that only one set of experimental data was used. This doesn't consider the fact that bubble growth and surface coverage would cause a non-uniformity in the consumption. Being consistent, the same data for the coal fuel source (as used in

previous sections) was used to approximate the consumption time in the anode. It only accounts for the time in which the carbon is active in the electrochemical process, not the additional time in which it is inactive in the anode. Running the carbon source at a higher overpotential would increase the rate of reaction, and thus increase both the consumption rate and the production rate of carbon, but still shows that the total time it takes to consume the particles is on the order of seconds. The assumption of a completely solid fuel source can be assumed by use of the coal densities, which account for the void spaces, thus producing an accurate carbon mass for each particle. With this knowledge, it is theorized that CO_2 bubble formation has the necessary time required to grow CO_2 bubbles that will cover the surface and reduce the electrochemical surface area.

4. Volume of Fluid (VOF) Model for CO_2 Gas Formation in a DCFC

4.1 Case Set Up

The analytical model presented in the preceding sections predicts that the formation of CO_2 gas bubbles on the carbon surface would limit the performance of DCFC's by reducing the electrochemical surface area. It however neglects two important elements to the physical model. It neglects the rate of bubble growth and the induced velocity field. If the gas bubble grows in a different fashion than was predicted, then the surface coverage may not be as affected. Alternatively, if the induced velocity field significantly influences the departure shape or size, then that may negate the issues associated with gas formation of the surface. To study these effects, a CFD model is created to more accurately predict the physics that occur within the DCFC anode.

This model is developed from the basic understanding of bubble growth initiated from a gas filled cavity. The case will be set up and run with the commercial software package available from ANSYS FLUENT (version 14.0.0). The preprocessing was initiated by creating the geometry and mesh in Gambit. The geometry consists of a simple horizontal surface, with an embedded cavity which is used to initiate the gas formation. The mesh will also be constructed with triangular cells to reduce the skew-ness and non-uniformity of the mesh, especially near the cavity region. Once a satisfactory mesh is generated, it is imported into FLUENT to continue the definition of the problem, including the required physics and boundary conditions. A sample two-dimensional geometry is shown in Figure 15.

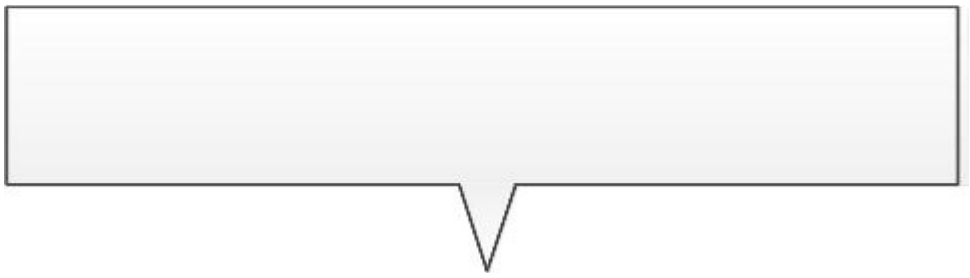

Figure 15: Sample geometry with boundary types

The geometry is two dimensional due to computationally cost. At the edge of the gas bubble, the mesh needs to be fine enough to capture the surface boundaries of the bubble, and a three dimensional bubble model would require a significant amount of computing power, with little increase in physical knowledge.

With the mesh imported into the FLUENT, governing physics (boundary conditions and governing equations) are defined. Since the bubble growth is time dependent, a transient case is constructed. The basic governing equations are the conservation of mass, momentum, and energy. However, the model is assumed incompressible and isothermal, so the conservation of energy can be decoupled from the conservation of mass and momentum. The solution of the remaining two conservation equations is important because the growth of gas has an effect on the velocity and pressure fields. The solution of these equations, when coupled with the effect of gravity and surface tension, will predict the bubble shape and departure more accurately than was described for a static bubble.

$$\frac{D\rho}{Dt} + \rho\nabla \cdot \vec{V} = 0 \tag{58}$$

$$\rho\frac{D\vec{V}}{Dt} = -\nabla \mathrm{P} - \nabla \cdot \tau + \rho\vec{g} \tag{59}$$

Since two separate phases are known to exist (liquid electrolyte and CO_2 gas), a multiphase model will need to be solved, in conjunction with the conservation of mass and momentum. In order to do this, the Volume of Fluid (VOF) model is added to the overall CFD model. This is a method of tracking individual immiscible fluids and the interface between them by adding a one scalar quantity per additional phase. That scalar is called the volume fraction (α), and is solved for each secondary phase. The solution to Eq. 60 would provide information about which phases are present inside a cell.

$$\frac{1}{\rho_q}\left[\frac{\partial}{\partial t}\left(\rho_q \alpha_q\right) + \nabla \cdot \left(\rho_q \alpha_q \vec{V}_q\right) = S_{\alpha_q} + \sum_{p=1}^{n}\left(\dot{m}_{pq} - \dot{m}_{qp}\right)\right] \tag{60}$$

The electrochemical reactions at the surface will be neglected, but the model will concentrate on the growth of a bubble by simulating this with a source term (S_{α_q}) that accurately adds carbon dioxide at the rate that it would be added if the cells was operating at the current density similar to that measured by Cherepy et al. (2005). To properly conserve mass, an equal amount of electrolyte mass will be removed from the liquid phase. Additional information about this model is provided in §*4.2 Description of the Volume of Fluid Model*.

Since the VOF model will be used to study the bubble growth and departure, the CO_2 and molten carbonate electrolyte are needed to be defined as separate phases. For an incompressible and isothermal model, the only fluid properties that are needed to solve the three governing equation (mass, momentum, and volume fraction) are the phase density, phase viscosity, and surface tension. The densities and surface tension were previously described in §*3.4 CO_2 Gas Departure within a DCFC*. The dynamic viscosity for the electrolyte mixture is also determined in a similar fashion, as Janz et al. (1963)

have measured the viscosity of the molten carbonate electrolyte. The viscosity measurements show that viscosity drops as the temperature increases, but does not measure the viscosity at any temperature higher than 600°C for a mixture. An estimate based on this work was taken to approximate the true viscosity of the molten carbonate electrolyte. The viscosity for gaseous CO_2 is taken by linear approximation from the experimental work of Fenghour et al. (1998), who experimentally measured the viscosity of CO_2 at temperatures up to 1500K. The values used in the model are provided in Table 6.

Table 6: Fluid properties used in VOF simulation of gaseous CO_2 growth

Molten Carbonate	Density	1900 kg/m^3
	Viscosity	$0.00207 Pa-s$
CO_2 Gas	Density	0.5242 kg/m^3
	Viscosity	$4.190 \times 10^{-5} Pa-s$
	Surface Tension	0.2 N/m

With the mesh, governing equations, and fluid properties now identified, the boundary and initial conditions can be defined. These are required to set the initial solution and subsequent boundary values for the governing equations. The initial conditions patch a gas bubble in the cavity using a User Defined Function (UDF), along with setting the pressure field to zero gauge pressure and a velocity field with zero magnitude throughout the domain. The boundaries are shown in Figure 15, where the bottom surface is a wall boundary which is impermeable to both fluids with a no-slip condition and a specified contact angle. The sides of the domain are modeled as symmetry boundaries, resulting in all normal gradients and velocity components equal to zero. The top of the domain is a pressure outlet to allow for escape of the gas bubble if it becomes detached. The pressure is set to atmospheric conditions, as would be seen in a DCFC anode compartment. With no inlet boundary and these basic settings, the only

induced fluid motion would be caused by the mass transfer of carbon dioxide to the bubble. Several cases will be presented to predict the gas motion in the domain.

4.2 Description of the Volume of Fluid Model

The phrase "Volume of Fluid" method was first coined by Hirt and Nichols (1981), and was used to track free boundaries in an Eulerian reference frame. This work was applied to many fluid problems in which discontinuities were present, such as shock waves and deformable bodies, in addition to multi-fluid problems. This allowed for the transient tracking of the interfaces, superior to many of the methods available at the time. Their work formed the foundation of the VOF model currently employed by ANSYS FLUENT.

The present volume fraction equation employed by FLUENT has added new surface tracking features and physics to the original VOF equation (ANSYS FLUENT, 2009). The current volume fraction equation (shown below as Eq. 60) contains the original conservation of volume fraction produced by Hirt and Nichols (1981), with the addition of the source and mass transfer terms on the right hand side. The volume fraction equation is used to calculate the volume fraction of only the secondary phases. When the VOF model is selected, one phase is defined as the primary phase, and all remaining phases are labeled as secondary phases, thus the primary phase is solved through the conservation of mass.

The mass transfer and source terms play a critical role in the solution of the volume fraction equation. In the presented case, the induced velocity field is created by the addition of the less dense gas phase, and a mass source term is added to each cell on

the interface. The interface is tracked through a User Defined Function that marks every cell with a volume fraction between ten and 95 percent. These limits are used to define what constitute a surface edge for a multitude of reasons. First, it does not add or subtract mass from cells that are completely filled with either phase. This is consistent with the generation of gas bubbles, where the mass transfer occurs on the edge of the bubble, and not within the bubble itself. Secondly, it protects the simulation form transferring mass in cells with a numerical rounding error, such as in the case where the volume fraction of molten carbonate is on the order of 10^{-5} somewhere far away from the bubble, producing erroneous mass transfer.

The magnitude of the mass transfer, which is dependent on the current drawn from the surface, will determine the value of the source term (or mass transfer terms if they are used). The value of the source term for phase 'q' is calculated by

$$S_{\alpha_q} = \frac{\dot{m}}{V} \tag{61}$$

where $\dot{m}$the mass transfer rate in kg/s, and V is is the volume of the cells where the source term is active. The units of the source term are kg/s-m^3, which is consistent with the other terms in the volume fraction equation. To determine the magnitude of this source term, a recorded current density from Cherepy et al. (2005) is used. In these experiments, when using coal as the carbon source, a current density of 65mA/cm^2 at 0.8V was achieved. Based on the electrochemical surface area (as was calculated in §*3.2 Determination of the Electrochemical Surface Area & CO_2 Evolution Rate)*, it has been shown that only about the coal derived carbon surface produced 10mA/cm^2, when based on the carbon surface area. Using this 10mA/cm^2, it was found that the carbon dioxide evolution rate was 8.04×10^{-8}mol/s per square centimeter of carbon surface area (this is

presented in Table 3). Converted into a mass transfer rate, that equates to 3.54 x 10^{-5} kg/s per square meter of carbon surface area. The reason for representing the evolution rate in these units is to easily modify the total mass transfer (in the numerator of Eq. 61) to be specific to the carbon surface geometry of the modeling domain. The mas transfer rate used in the numerator can be calculated by multiplying the virtual surface area by the carbon dioxide evolution rate as defined in Table 2.

$$\dot{m} = \left(3.54 \times 10^{-5} \frac{kg}{s - m^2 C}\right) A_{CFD} \tag{62}$$

Combining this redefinition of mass transfer and the source term, then the source term would, in theory, be defined as:

$$S_{\alpha_q} = \frac{\left(3.54 \times 10^{-5} \frac{kg}{s - m^2 C}\right) A_{CFD}}{V_{CFD}} \tag{63}$$

This source would be added to the simulation in each cell on the interface to simulate the accurate amount of carbon dioxide transfer into the solution. However, in practice, this does not occur. Since the mass transfer occurs only on the surface (as was tracked by the UDF), the volume in the denominator changes with every time step, resulting in a source term that changes with each time step. Due to this fact, the source term cannot be calculated based on the entire geometric volume. Instead, an iterative method is used in each case to determine what value the source term requires to obtain the mass transfer rate as described in Eq. 62. The details are described in each case.

Properties in the VOF model are defined according to the phase volume fraction. FLUENT uses a volume fraction averaging method to determine the cell center's material properties, as shown in the following equation for calculating the average density:

$$\rho = \sum_{q=1}^{n} \alpha_q \rho_q \tag{64}$$

All material properties, including viscosity, are calculated in this manner, so that when a cell is completely filled with a single phase, the average density is equal to that phase density. However, in the case that a cell is only partially filled, then the VOF model reconstructs the surface to approximate the face fluxes.

The volume fraction equation can be discretized either by using an implicit or an explicit scheme. The implicit scheme solves for the volume fraction of each secondary phase at the current time step by iteration. A finite-difference interpolation scheme is used to calculate the face fluxes at all cells, even those that exist on or near a phase boundary. The explicit scheme solves for the current volume fraction by utilizing the previous time step's volume fraction. This scheme is shown in Eq. 65 (ANSYS FLUENT, 2009).

$$\frac{\alpha_q^{n+1}\rho_q^{n+1} - \alpha_q^n \rho_q^n}{\Delta t} + \sum_f \left(\rho_q^n U_f^n \alpha_{q,f}^n\right) = \left[\sum_{p=1}^{n} \left(\dot{m}_{pq} - \dot{m}_{qp}\right) + S_{\alpha_q}\right] V \tag{65}$$

Here, the current volume fraction (α_q^{n+1}), depends on the face fluxes from the previous time step ($\rho_q^n U_f^n \alpha_{q,f}^n$), along with the mass transfer and source terms. In order to do that, FLUENT first calculates the face fluxes, dependent on the choice of interface treatment.

When selecting the volume fraction discretization scheme, there are two approaches to interpolating the face fluxes. The first option is to reconstruct the interface using a technique that approximates the edges of the fluids then calculates the face fluxes. Alternatively, a finite volume approach could be used to calculate the volume fraction (ANSYS FLUENT, 2009). In the following models, an interface reconstruction for the

explicit scheme is done through a process called Geo-Reconstruct, which is based on the work of D.L. Youngs (1982). This scheme solves the geometry of the phase interface then uses that information to calculate the face fluxes, which is then in turn are applied to the volume fraction equation to calculate the next time step's volume fraction. When the process is finished, each cell with a volume fraction between zero and one should have a linear boundary separating the phases. Within the cell, to begin the process, the slope of the linear boundary is a function of the face volume fractions on the cell's four faces (north - f_N, south - f_S, east - f_E, and west - f_W). This is visualized in Figure 16, while the slope is calculated in Eq. 66. It can be extended into more than two fluids.

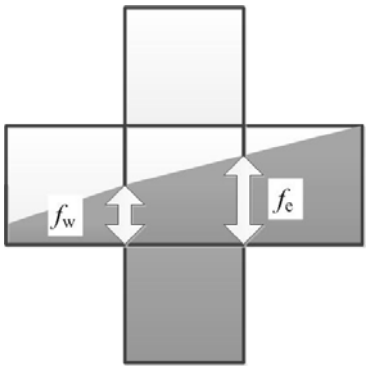

Figure 16: Visualization of the reconstruction of the interface

$$slope = \frac{f_E - f_W}{f_S - f_N} \qquad (66)$$

With knowledge of the slope, the position of the linear interface is determined by the current time step's phase volume fraction within the cell. This position is used to determine the percent of each phase on the cell faces, and then the face fluxes can be determined based on the fraction of each phase that is present on said face. A completed interface is shown for a rectangular mesh in Figure 17.

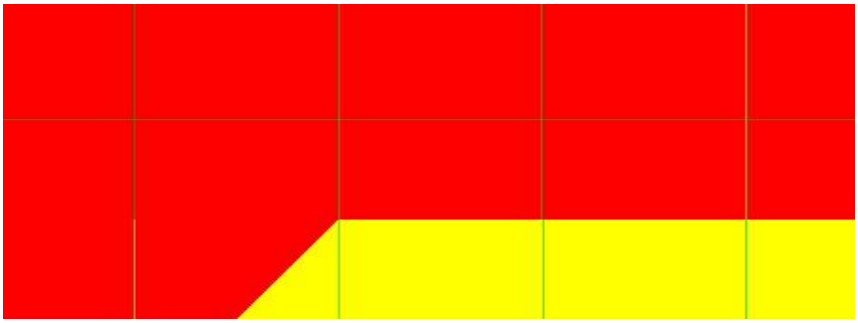

Figure 17: A phase boundary as reconstructed with the Geo-Reconstruct method

As time marches on, these face fluxes are then applied to the calculation of the next time step's volume fraction, and the interface tracking procedure repeats itself until the solver is terminated.

To complete the VOF model, surface tension and wall adhesion must be defined. The surface tension force used in FLUENT (2009) was originally introduced by Brackbill et al. as a source term in the momentum equation. Since the surface tension is assumed constant in this isothermal case, the surface normal of the gas bubble is determined by the gradient of the volume fraction:

$$\vec{n} = \nabla \alpha_q \tag{67}$$

FLUENT then calculates the unit normal vector of this vector:

$$\hat{n} = \frac{\vec{n}}{|\vec{n}|} \tag{68}$$

in order to determine the curvature of the bubble by Eq. 69:

$$\kappa = \nabla \cdot \hat{n} \tag{69}$$

For the case where only two phases are present, then $\kappa_p = -\kappa_q$ and $\nabla \alpha_p = -\nabla \alpha_q$, resulting in the surface tension force being calculated as:

$$F_\sigma = \sigma_{pq} \frac{\rho \kappa_q \nabla \alpha_q}{\frac{1}{2}(\rho_p + \rho_q)} \tag{70}$$

In order to capture the effects of the contact angle, the contact angle must be defined with the application of the wall adhesion option in FLUENT (2009). Since the contact angle is not defined in the surface tension force (Eq. 70), it must be applied near the wall to affect the calculation of the curvature. The method to implement this condition was also introduced by Brackbill et al. and creates a "dynamic boundary condition." By specifying the contact angle in the boundary conditions tab, the cells next to the wall boundary have their surface normal changed according to:

$$\hat{n} = \hat{n}_w \cos\theta_w + \hat{t}_w \sin\theta_w \tag{71}$$

where $\hat{n}_w$ and $\hat{t}_w$ are unit vectors defined in the normal and tangential directions of the wall. This is used to calculate the curvature of the surface where two phases meet.

4.3 Validity of the VOF Model towards Case

The VOF model was created to track free boundaries in a number of cases. But, in order to use it, it must be shown that the VOF model is applicable to growth of CO_2 gas bubbles in the anode compartment of a DCFC. The modeling physics does not capture the entire governing physics and chemistry, but it is able to capture the physics of the bubble motion. Neither the molar concentration of carbon dioxide in the electrolyte solution nor the consumption of the carbon fuel is modeled. Instead, the current density is assumed constant, allowing carbon dioxide to dissolve into the electrolyte. By assuming the electrolyte solution to be saturated with carbon dioxide, the correct amount of mass transfer can be added into the gas phase. Based on the long consumption times found in §*3.5 Coal Consumption Timescale*, the fixed surface approximation can be used on much

smaller timescales. Of the many multiphase tracking methods, the VOF model was chosen for a variety of reasons.

The primary usage for the VOF model was to track free-boundaries in which discontinuities are present, as well as mobile. It allows the two fluids to move in an Eulerian reference frame while successfully tracking the fluid regions, before approximating the boundaries. All that is required is that the two fluids are immiscible and not "interpenetrating" (ANSYS FLUENT, 2009).Based on the case set up, the two prescribed phases adhere to both of these requirements. When the electrolyte is fully saturated, the carbon dioxide will exit into the predefined vapor pockets, and these two materials will not mix. The governing physics then reduces to the complete force balance on the gas bubble, as had been described in §*3.4 CO_2 Gas Departure within a DCFC.* The remaining requirements described in the ANSYS FLUENT manual (2009) are all related to the numerical setup, and thus are obeyed in creating each case.

4.4 VOF Results for a Non-Wetting Surface (θ = 140°): Millimeter-Scale

The first case to be analyzed is the growth of carbon dioxide on a non-wetting surface, where the contact angle between the surface and the electrolyte is 140°, which may be high for carbon, according to some estimates; however it still demonstrates the role of a non-wetting surface. In an effort to examine both the effect of contact angle and cavity angle, two separate geometries are studied on a millimeter scale, one with a cavity half angle of approximately 76° (and a 20cm length), and another with a 20° half angle (with a 10cm length). These two geometries are shown in Figure 18.

Figure 18: Geometry for two different nucleation sites (right, ϕ = 76°; left, ϕ = 20°)

In each of these geometries, an initial gas bubble was patched in the cavity to initiate the mass transfer. Based on the virtual surface area of the carbon surface, the predicted carbon dioxide growth rate was calculated for 10.34mA/cm^2 current density (as was determined in *§3.2 Determination of the Electrochemical Surface Area and CO2 Evolution Rate*). These rates are shown in Table 7.

Table 7: CO_2 mass transfer rates for each geometry based on drawing 10.34mA/cm^2 from the surface

Cavity Half Angle	Length	CO_2 Evolution Rate
20°	10cm	3.77×10^{-7} kg/s
76°	20cm	7.08×10^{-7} kg/s

Since the mass transfer occurs on the surface of the bubble, the numerical mass transfer rate is a moving target, as had been stated in *§4.2 Description of the Volume of Fluid Model*. This occurs because as CO_2 is evolved out of solution and the bubble grows, its surface expands, increasing the number of cells actively generating CO_2. To control the rate of bubble growth, a local and an average mass transfer rate were calculated based on the previous time step's CO_2 mass and initial CO_2 mass respectively:

Local Mass Transfer Rate
$$\dot{m}_{local} = \frac{m_{v,n} - m_{v,n-1}}{t_n - t_{n-1}} \quad (72)$$

Average Mass Transfer Rate
$$\dot{m}_{average} = \frac{m_{v,n} - m_{v,o}}{t_n} \quad (73)$$

These mass transfer rates were monitored between one and four times each millisecond for each of the five cases that are presented. This leads to the bubble growing at the approximate rate that it would in the real physical case. By careful monitoring for these

values, the mass transfer rates were decreased as the bubble grew to maintain the CO_2 evolution rates described in Table 7. If the mass transfer rates were not controlled, and were too high causing the bubble to grow too fast, the velocity field would be overestimated, and the results would inaccurately depict forces affecting departure.

After each case was set up properly and run for hundreds of thousands of time steps, the results were post-processed and are presented here. Confirming the analytical and experimental results of Chapter 3: *Physical Model Analytical Results*, the non-wetting characteristics of the surface causes the gas phase to spread along the surface limiting the access of oxide ions to the surface. The results for the cavity with a half angle of 76° are shown in Figure 19, while the average mass transfer rate is plotted in Figure 20:

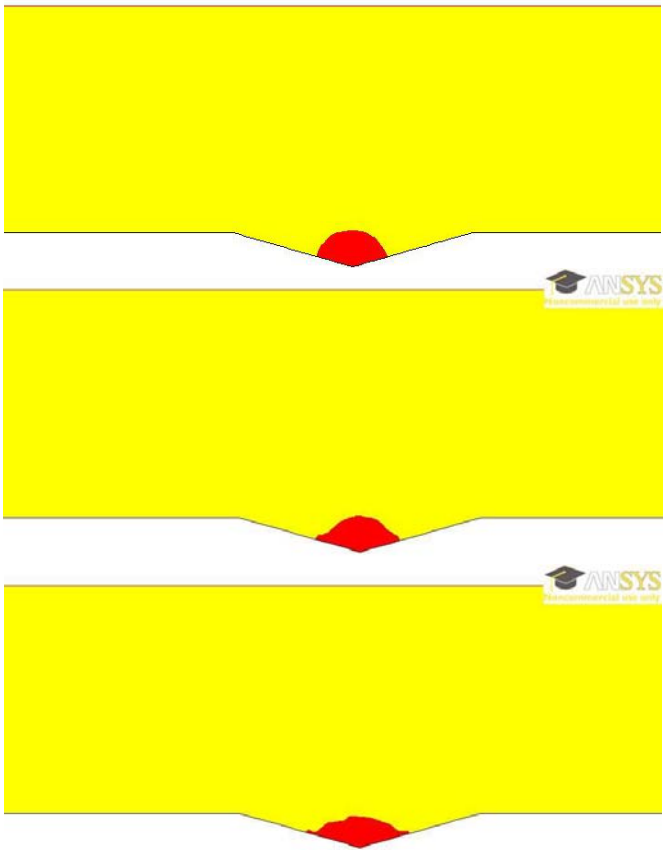

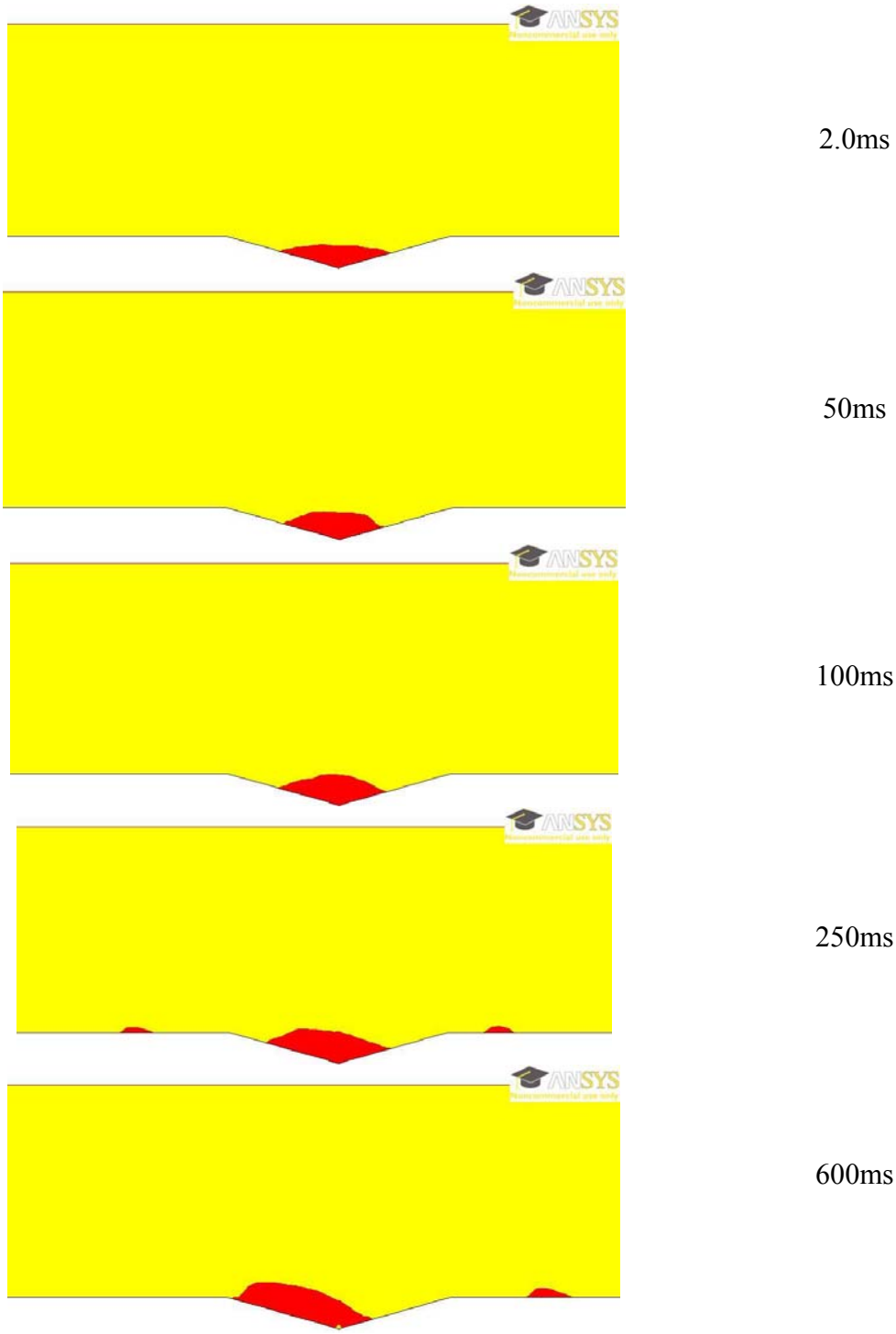

Figure 19: CFD model showing the spreading and growth of a CO2 gas bubble (in red) in a molten carbonate electrolyte (yellow) on a millimeter scale with a contact angle of 140°. Note the spreading of the initial gas bubble inside the cavity (ϕ = 76°)

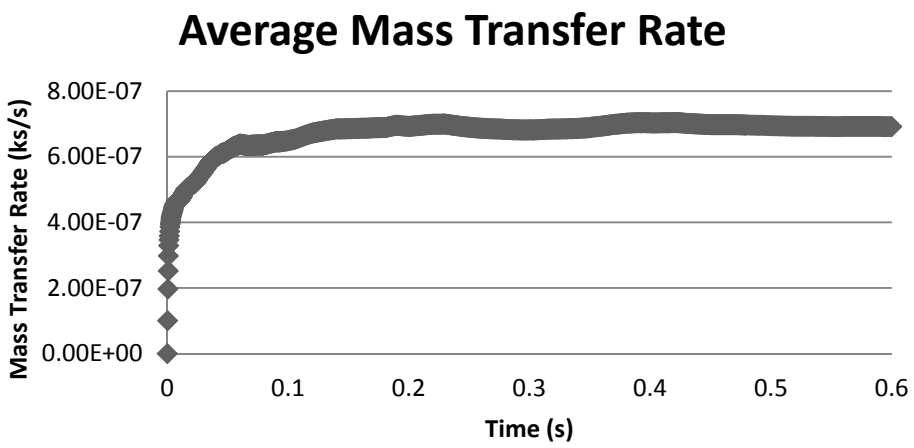

Figure 20: Average CO2 evolution based on the initial mass indicating that during the simulation, the numerical mass transfer matched the theoretical mass transfer, deviating by only 2.2%

From Figure 19, the physics of the gas phase generation generally matched the analytical physics from §*3.4 CO_2 Gas Departure within a DCFC* and the observed physics of Phan et al. (2009), and Takata et al. (2010) in §*3.3 Hydrophobic Boiling Process: an Analogy to CO_2 Bubble Growth*. As was observed with boiling water on a hydrophobic surface, as CO_2 evolved from solution, it increased the size of the gas bubble. That increase in volume lead to the spreading of the gas phase over the surface. In the first 600ms, the gas bubble effectively doubled its length coverage, expanding from initially covering 1mm to covering over 2mm of the 20mm length of the surface. However, this does not produce the predicted spherical shape that was predicted. This is because of the large cavity region. As the bubble tends to be leaning toward the left of the simulation, it makes a contact angle of 140° with the left side of the wall; however, it is also slightly in contact with the right wall, requiring that the contact angle also be 140° at that edge. To compensate for that change in surface geometry, the bubble takes an irregular shape with changes in its concavity. The bubble attempts to find a flat surface to minimize the surface area, causing it to crawl up one of the sides. Eventually, should this

case be run for a long enough period of time, the bubble would come to rest on the flat left wall, where it can smoothly spread as a spherical cap.

At no point of the simulation does the bubble in Figure 19 attempt to depart the surface. This trait is shared with the sharper cavity, with a 20° half angle. The results for this geometry are shown in Figure 21.

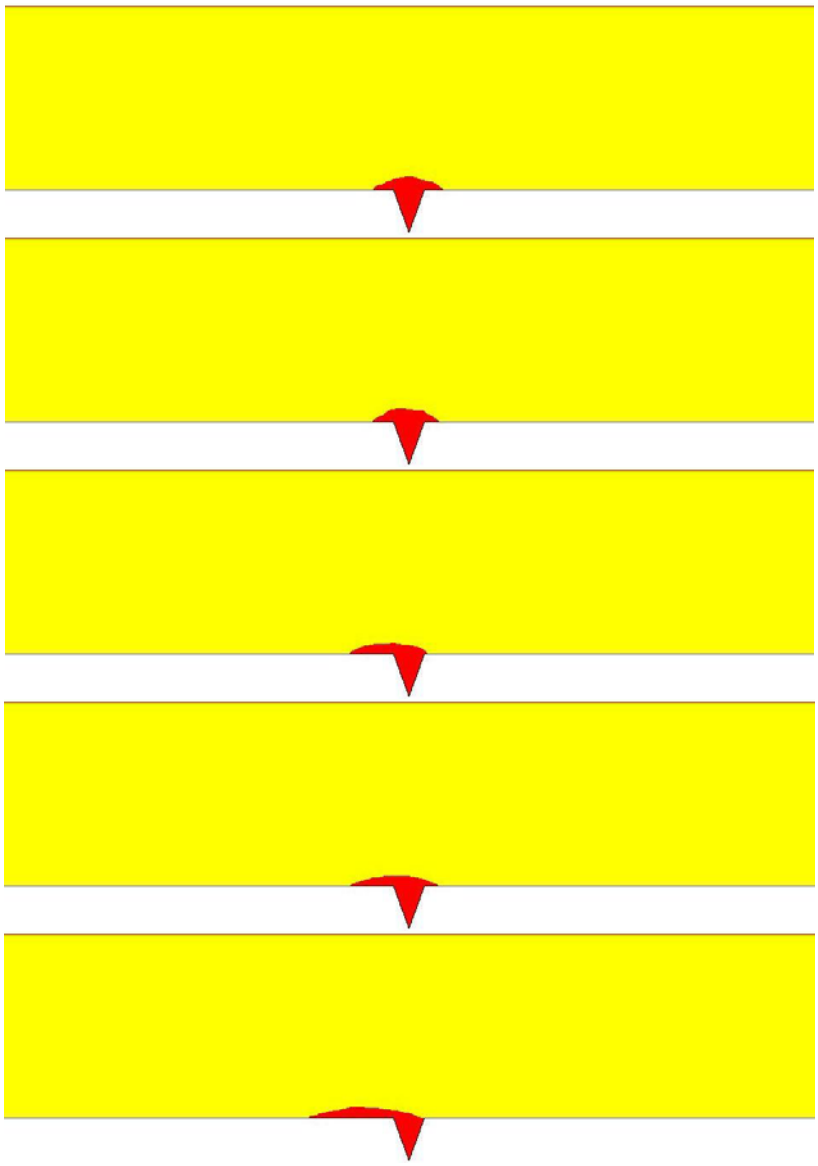

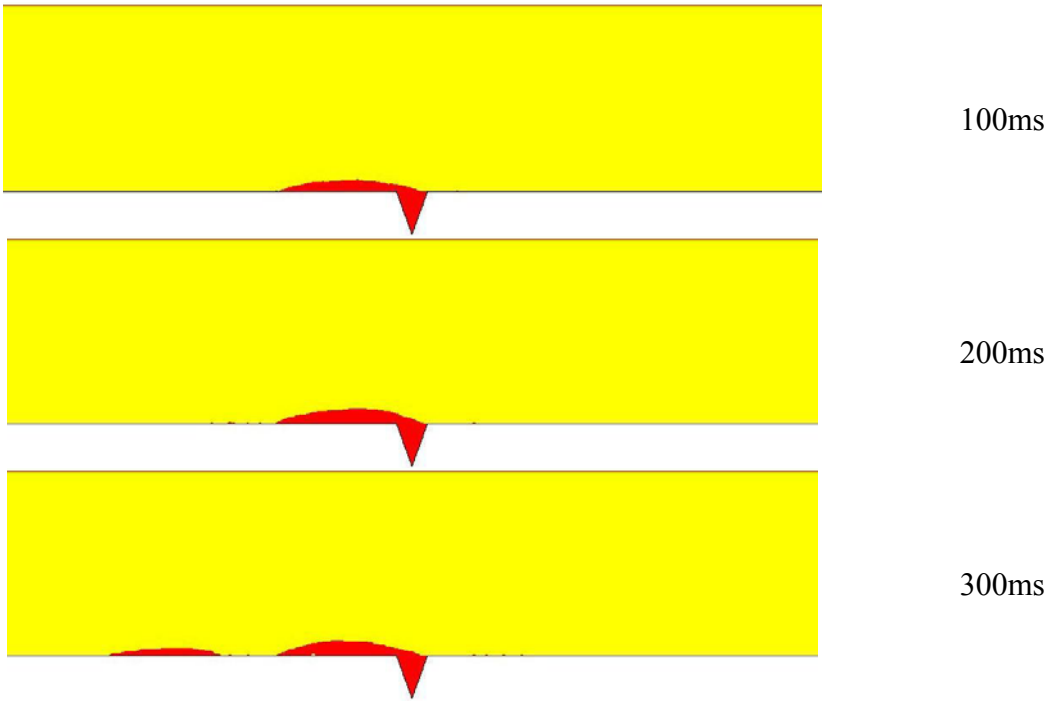

Figure 21: CFD model showing the spreading and growth of a CO2 gas bubble (in red) in a molten carbonate electrolyte (yellow) of length 10mm. Note the spreading due to the 140° contact angle.

Though this only depicts half the time (300ms, compared to 600ms for the geometry in Figure 19), the physics is again a match to both the analytical and experimental observations. The bubble grows as CO_2 exits solution and its shape is governed by the contact angle, producing a nearly perfect spherical gas cap, due to its presence on a relatively flat surface.

To fully understand the mechanisms at work in these models, a deeper look is given to the governing physics. Beginning with an initial gas bubble, the surface tension force and wall adhesion act to change the bubble shape to conform it to the surface contact angle in the first few time steps. As time advances, and the bubble grows, the contact angle determines the bubble curvature at the wall, which helps define the curvature of the remaining surface. This curvature is then used in the calculation of the surface tension force (Eq. 70), which then is added to the momentum equation (Eq. 59) as

a source term. The mass transfer out of solution causes a small velocity field which could either help (inertia) or hinder departure (drag). Buoyancy effects are added to the calculation to predict departure. In these two cases, as was consistent with the previous theory, the small volume of the cap does not produce enough buoyancy to overcome the surface tension force and initiate departure. This leaves the gas bubble attached to the surface effectively blocking the electrochemical surface area.

4.4.1 Author's Note

This section is a quick note about some of the features observed in the previous CFD results and the results with will follow. There are three issues which should be stated before more work is presented.

The first issue relates to the geometry. In a two dimensional geometry, there is no influence from a third dimension (i.e. the z direction). This means that the gas region effectively extends infinitely in that direction, without a front or back to the bubble. This means that the spherical geometry departure sizes from the analytical work cannot be directly related to the numerical results. The unrealistic shape would change the surface tension calculation, as well as the buoyant force. However, the mass transfer term would not be effected, since the surface area and volume are both a function of the depth. This depth would cancel out in the determination of the source term (Eq. 63), so an accurate two dimensional growth rate can be depicted. Future work should use a three dimensional geometry that models the true shape of the gas bubble.

The second issue with these models comes with the choice of using the Geo-Reconstruct scheme to model the surface. The advantage of using this model is that is has a high powered surface reconstruction, which would be helpful in determining the shape

of the bubble. However, as can be seen in the last image of Figure 19 (at 600ms), and will be seen in the upcoming wetting surface results, there are erroneous cells with incorrect volume fractions. In the last image of Figure 19, only one cell has an incorrect volume fraction, so it can be hard to see, but this is more prevalent in the wetting surfaces where the electrolyte can creep into the cavity. These cells are unrealistic and can cause the model to predict inaccurate physics in certain cases.

The last issue is related to the numerical error. As can be seen after 250ms in both hydrophobic cases, there are additional gas bubbles on the surface. These are created as the bubble expands and the source term is added to additional cells. In cells near the surface where the gas phase has been inserted to produce a volume fraction (α) of approximately 10% CO_2, those cells are then allowed to them to produce additional gas, even if they were not a true part of the bubble. This small gas cell then grows and produces as an entirely separate bubble. Further refining of the mesh or mass transfer UDF could help alleviate this problem by reducing the number of cells inaccurately contributing to the gas growth.

4.5 VOF Results for a Wetting Surface (θ = 10° and θ = 50°): Millimeter Scale

In contrast to the non-wetting carbon surface, the wetting surface should produce vastly different physics. Nucleate boiling generally occurs on hydrophilic surfaces with low contact angles when the heat flux is les then the critical heat flux (CHF). This results in a smaller surface tension force holding bubbles attached to surface, and acting against buoyancy. Since water vapor bubbles tend to bead up on a wetting surface, there is sufficient volume to overcome surface tension and initiate departure. This phenomenon

was also analytically predicted to occur in the case of CO_2 gas bubbles that sit on highly wetting carbon surfaces (see §*3.4: CO_2 Gas Departure within A DCFC*). The governing physics and material properties remained the same, the only change occurred with the surface contact angle, and showed that if the carbon surface was wetting, that surface area coverage would not be a major loss in the system.

Two different cases were run using the same geometries of Figure 18, but with different contact angles. For the larger cavity (ϕ = 76°), a contact angle of 10° was modeled which should show complete departure of the entire gas bubble and removal from the domain. The sharper cavity (ϕ = 20°), had a wall contact angle of 50°, which should allow for the gas bubble to partially depart. Due to the contact angle exceeding the total cavity angle (50° compared to 40°), a small portion of the CO_2 gas should remain and become a nucleation site for future bubbles. The results for the larger cavity (ϕ = 76°) are shown in Figure 22.

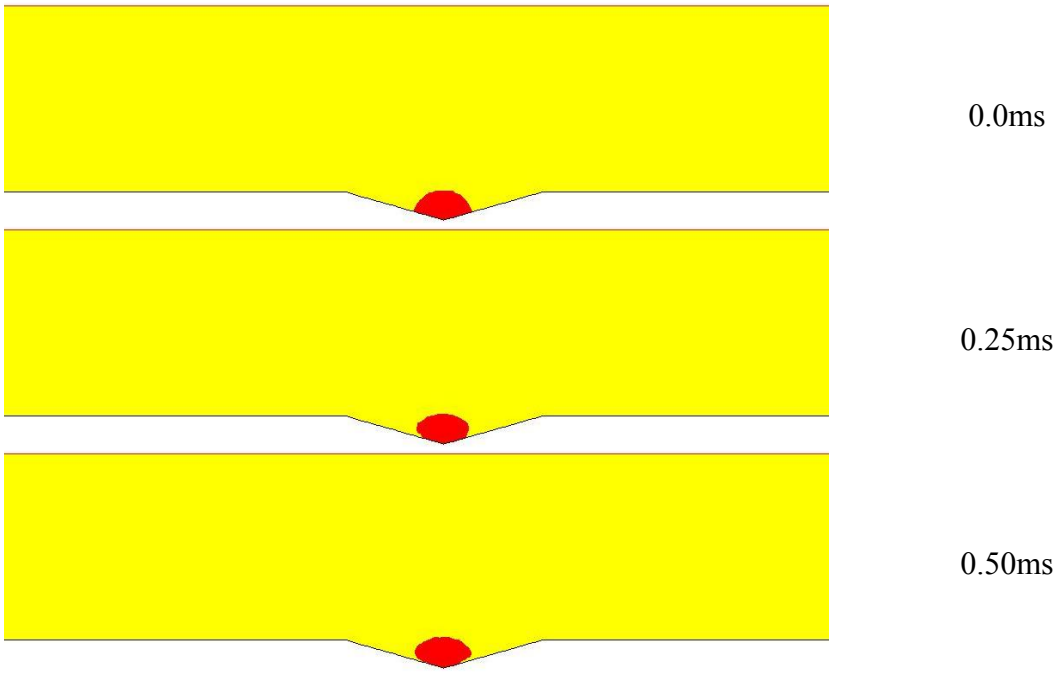

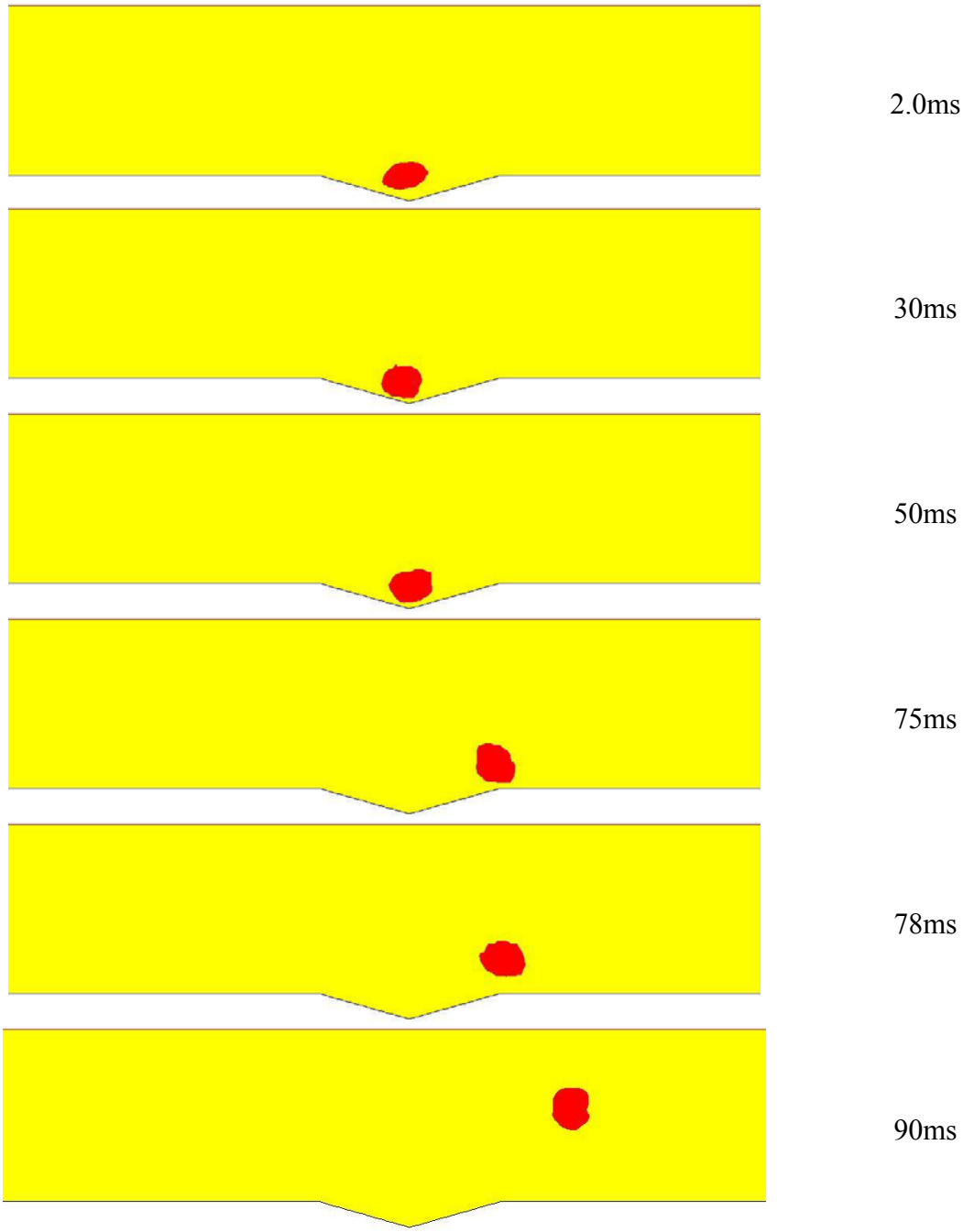

Figure 22: Results for a CO_2 gas evolution on a non-wetting surface (θ = 10°)

The results from this case produce interesting observations. Overall, the gas bubble detaches quickly (within the first 2ms) and eventually departs the surface (around 78ms). However, in between, the gas bubble appears to hover over the surface, approximately

one cell from the wall. This can be explained by examining the volume fraction near the surface, as shown in Figure 23.

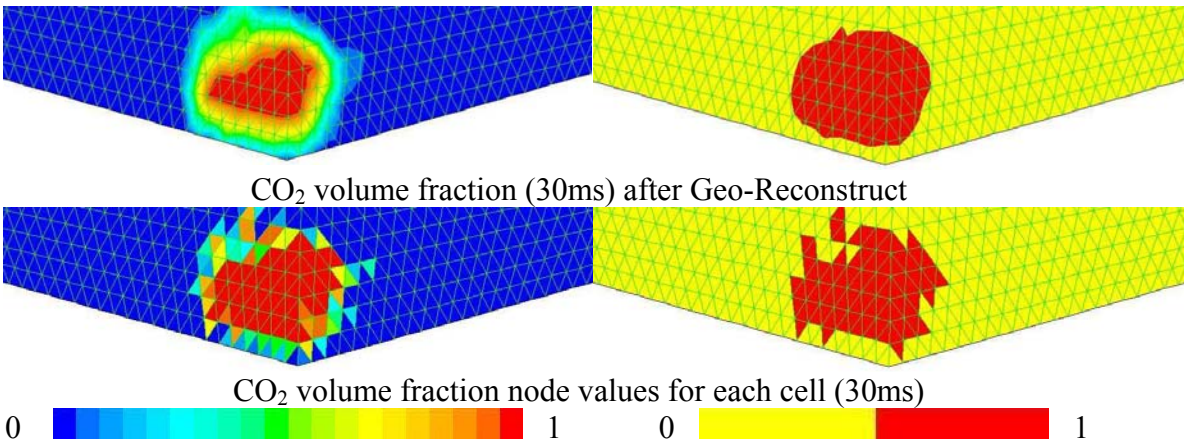

Figure 23: Cell values for the CO2 volume fractions showing slight attachment of the bubble to the surface

Upon closer inspection of the CO_2 volume fraction near the wall at 30ms, it is shown that there are still a small number of cells with a fraction of gas that are still attached to the surface. These cells seem to be contributing a small surface tension force that allows the bubble to remain attached. It is not until 78ms, when the gas bubble is carried along to the top of the right side of the cavity, that it actually detaches and exits the domain. This appears to be a limitation of the surface tension and VOF model to predict departure in this case. However, when the bubble rose up the surface of the cavity, and encountered a flat surface, did it eventually depart. The same situation is seen with the sharper cavity, as depicted in Figure 24:

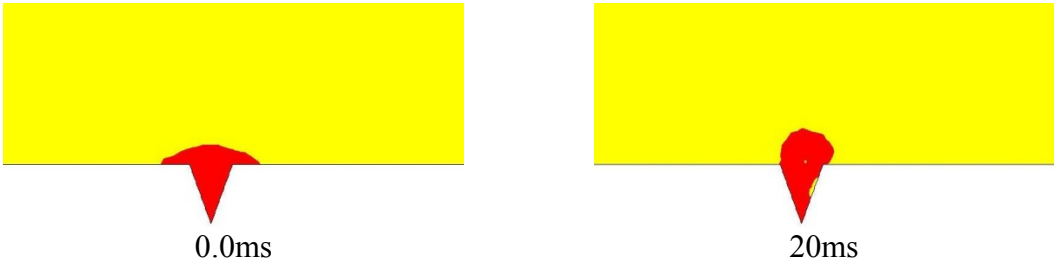

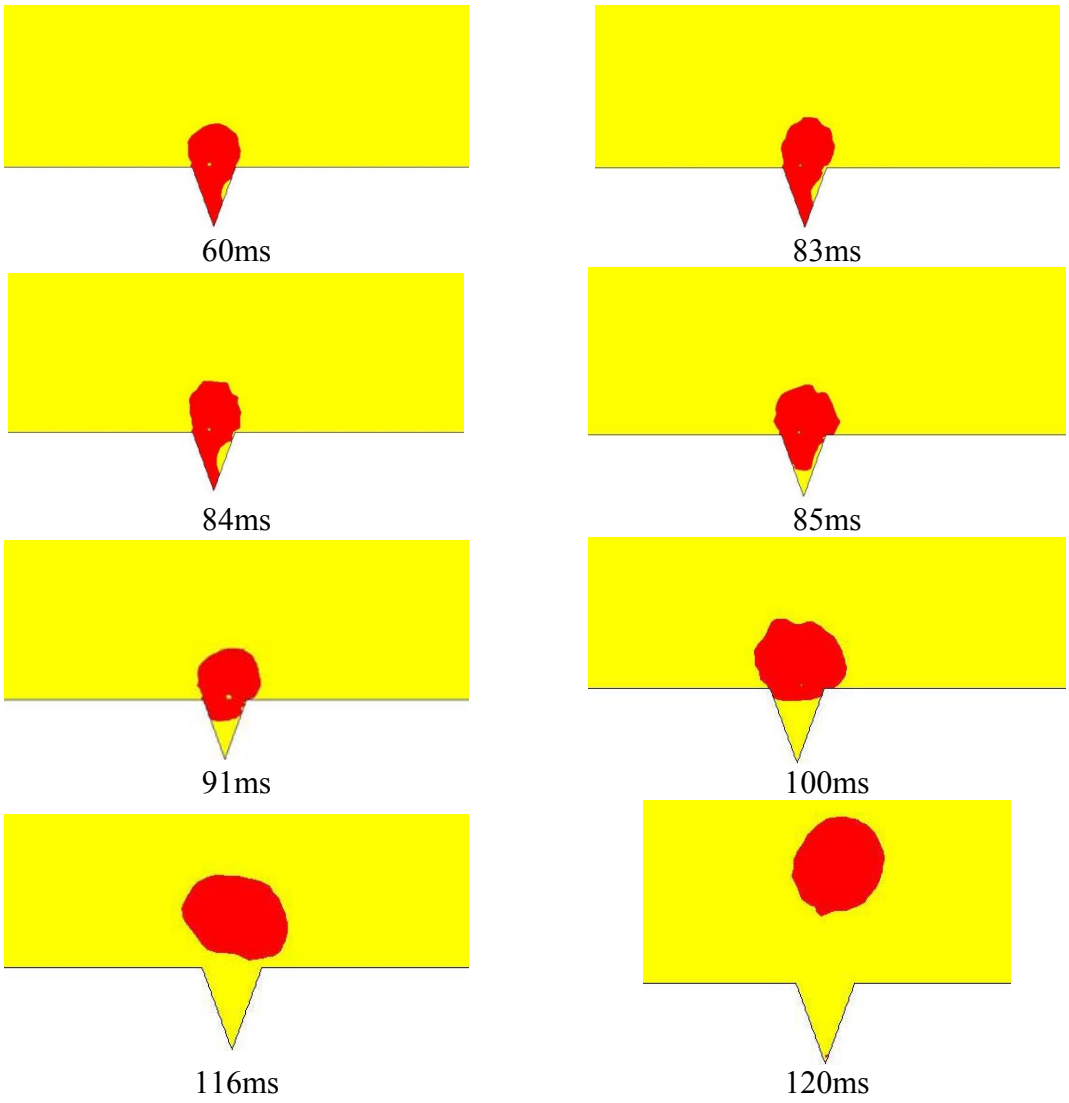

Figure 24: CO_2 bubble departure from a wetting surface (θ=50°)

This result also has quite a few interesting features to it. From looking at the gas bubble, this is the first result in which the Geo-Reconstruct method places a significant number of cells filled with molten carbonate directly in the region where it should not be. It is first seen at 20ms, where a small area on the right cavity wall indicates the presence of molten carbonate. At no point does molten carbonate begin to penetrate the cavity until 80ms, when the buoyant forces are sufficient to begin lifting the bubble off the surface. Until this time, the Geo-Reconstruct method is improperly placing molten carbonate in that region. After that point, the molten carbonate then begins to seep into the cavity and

begin removing the bubble from the surface. But, another problem is encountered, where the surface tension holding the bubble together appears too high. This results in the entirety of the gas being removed from the domain, rather than a small amount that should be left inside the cavity to continue nucleation.

The overall results are still meaningful, regardless of the problems encountered. For a highly wetting surface ($\theta = 10°$), and even for a less wetting surface ($\theta = 50°$), the buoyant forces are sufficient to exceed the surface tension forces and remove the gas from the surface. Larger bubbles are required to detach from surfaces with a higher contact angle, but detachment is still possible (unlike the non-wetting surfaces), and their growth pattern allows for much less surface coverage during their period of growth. Thus, for wetting surfaces in a DCFC, the effect of the predicted mass transport losses may hold also. Ultimately, the surface of carbon appears to be non-wetting, leading to the idea that CO_2 bubble growth presented in the preceding section is more likely to affect cell performance. However, if the contact angle between the carbon and electrolyte can be reduced, mass transport losses may be less prevalent, at least on larger particles. This contact angle would need to be sufficiently wetting though, as will be shown in the following section.

4.6 VOF Results for a Slightly Wetting Surface ($\theta = 80°$): Millimeter Scale

This final case shows the physics of a slightly wetting surface ($\theta = 80°$), By definition, the surface is wetting (i.e. $\theta < 90°$), albeit, only slightly. Referring back to Figure 14, a large amount of gas is required to remove a CO_2 bubble from slightly wetting to neutral surface. While the covered surface area is not the largest, the volume

would still cause the gas bubble to remain attached to the surface for a significant period of time, thus limiting the electrochemical surface area for a substantial interval. The sharp cavity geometry is used in this model, and the results are presented in Figure 25.

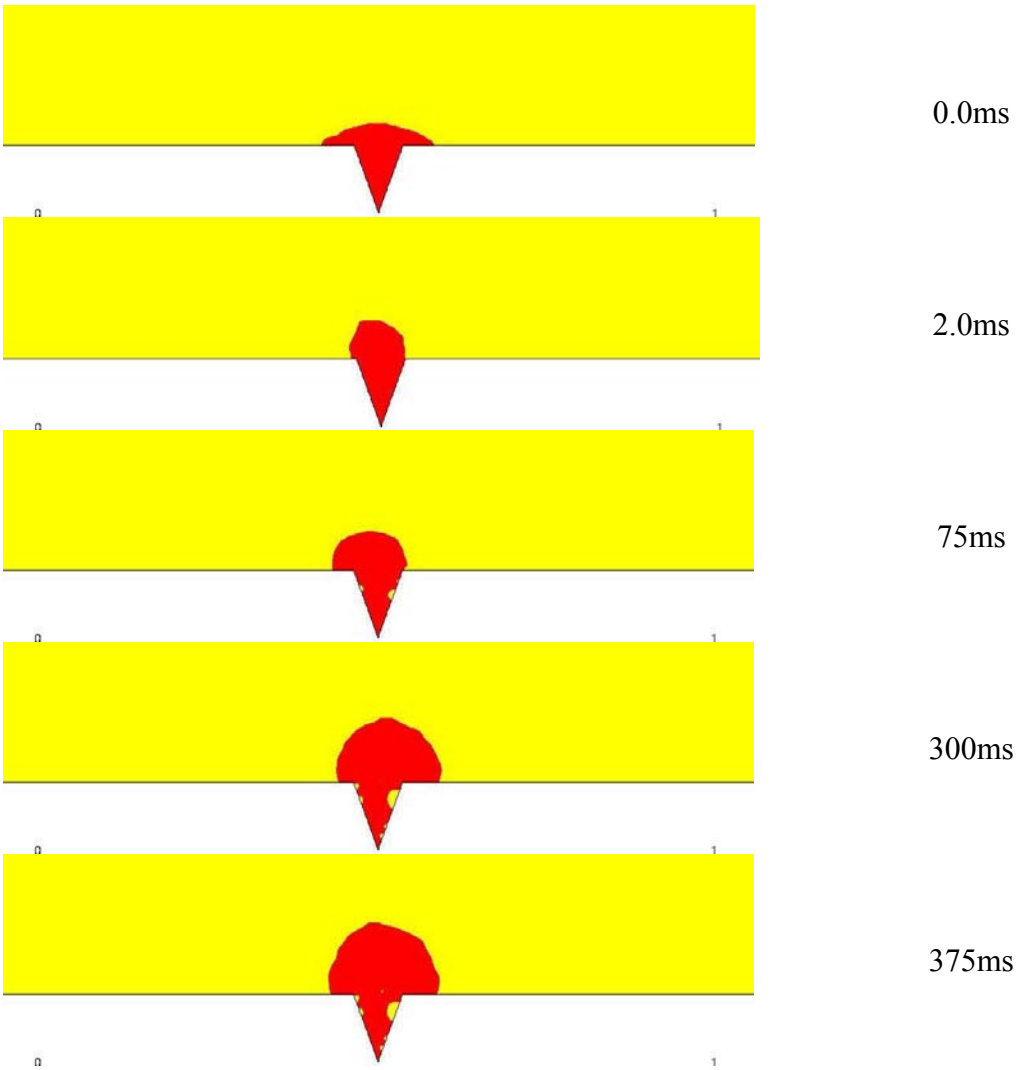

Figure 25: CO_2 bubble growth on a slightly wetting surface (θ = 80°)

Again, Geo-Reconstruct incorrectly adds molten carbonate into the gas bubble; however, the timescales provide an interesting product. For surfaces with a higher degree of wettability, the gas would have departed from the surface before 100ms. Now, because more gas is required to detach the bubble, the time and surface coverage required before departure is increased. Assuming that this bubble could be run to departure, then both a

significant amount of time and surface area would be covered. In this case, a large bubble may not be as influential as a bubble on a non-wetting surface, nor will it never depart. This bubble may depart, but not before blocking some of the electrochemical surface area for an extended time, thus this could be just as hindering as a non-wetting surface, especially is multiple bubbles appear on the surface.

5. Conclusions

An evaluation of the current research regarding DCFCs shows a lack of understanding about performance losses due to mass transport limitations. We have attempted to explain the physics behind the mass transport losses from a fundamental standpoint. By showing that the electrochemical surface area is much larger than the electrode surface area, the true current density (based on the electrochemical surface area) shown that is can be comparable to the amount of current produced on platinum, depending on the layers of carbon active in the oxidation reaction. But the CO_2 production rate can still oversaturate the electrolyte solution. In an attempt to understand the mass transport losses, an analogy was drawn to boiling on a hydrophobic surface. Experimental observations reveal that hydrophobic surfaces cause gas bubbles to spread and merge bringing forth film boiling. The critical comment about this process is that no individual bubble was able to depart from the surface.

Carbon surfaces were researched and found to be non-wetting, particularly for molten carbonate solutions used as electrolyte in many DCFCs. The exact level of non-wettability has not been measured in a molten carbonate solution, but allows for the hydrophobic surface analogy to be applied. An analytical force balance showed that CO_2 gas bubbles could depart at only a single size and shape for every contact angle. Wetting surfaces required little volume to depart, while non-wetting surfaces required up to hundreds of square millimeters of surface coverage before departure would even be remotely possible. ANSYS FLUENT was used to confirm this in a two dimensional geometry. Wetting surfaces required small volumes of CO_2 before departure, while non-wetting surfaces were unable to depart at all. The gas instead spread along the surface,

covering it with a film of CO_2 gas. The physics of gaseous CO_2 growth matched the physics of hydrophobic boiling. This means that the surface features of carbon play a significant role in the mass transport losses.

Surface coverage equates to a loss in electrochemical surface area. Since the carbon oxidation occurs directly at the carbon surface when the carbonate ion reacts with carbon and resulting electrons are carried away in the electrically conductive phase, covering the carbon surface with CO_2 effectively eliminates a portion of available carbon, rendering it inactive. This is similar to flooding in a PEM fuel cell, where liquid water in the cathode can block oxygen access to the platinum catalyst. By covering the carbon surface, the carbonate ion, which is required for carbon oxidation, cannot reach the surface. Solutions to this problem include modifying the carbon surface to change its wettability or a more proficient removal of carbon dioxide.

Appendix A: Molten Carbonate and CO_2 Properties

This appendix lists the actual properties for individual molten carbonates (i.e. Li_2CO_3, Na_2CO_3, and K_2CO_3) and gaseous CO_2 that were published in the literature, and referred to in the text.

Note that Temperature (T) in °C

$t = (T + 273.15)/1000$

Lithium Carbonate: Li_2CO_3

Property	Formula	Units
Atomic Weight	73.89	g/mol
Surface Tension	$0.001[273.6 - 0.0407T]$	N/m
Density	$2126.33exp[-(2.0659 \times 10^{-4})T]$	kg/m^3
Viscosity	$(4.1046 \times 10^{16})T^{-5.8642}$	Pa-s
Specific Heat	$\frac{1}{M}[185435 - 0.051t + 0.03t^2 - 0.006t^3 - 0.003t^{-2}]$	J/kg-K

Sodium Carbonate: Na_2CO_3

Property	Formula	Units
Atomic Weight	105.988	g/mol
Surface Tension	$0.001[255.8 - 0.0514T]$	N/m
Density	$2405.5exp[-(2.3142 \times 10^{-4})T]$	kg/m^3
Viscosity	$1186.4exp[-0.009202T]$	Pa-s

Specific Heat	$\frac{1}{M}[189535 - 0.007t + 0.002t^2 - (5.2051 \times 10^{-6})t^3 - 0.003t^{-2}]$	J/kg-K

Potassium Carbonate: K_2CO_3

Property	Formula	Units
Atomic Weight	138.204	g/mol
Surface Tension	$0.001[226.9 - 0.0642T]$	N/m
Density	$2344.9exp[-(2.3633 \times 10^{-4})T]$	kg/m^3
Viscosity	$2415.56exp[-0.009812T]$	Pa-s
Specific Heat	$\frac{1}{M}[209200 - (1.629015 \times 10^{-4})t + (8.00985 \times 10^{-5})t^2 - (1.33643 \times 10^{-5})t^3 - (2.1053 \times 10^{-5})t^{-2}]$	J/kg-K

Appendix B: Supplemental Mathematics for Gas Bubble Departure

This appendix contains the geometric proof for determining the gas bubble volume based on a known relationship for the volume of a spherical cap. Also included are the two remaining cases (wetting surface and a neutral surface)

B.1 Geometric Proof

This appendix assumes the knowledge of only two geometric quantities, the chord of a circle (of length d_b) and the angle, θ, formed between the chord and a tangent line of the circle (labeled *T*). The circle is labeled *C* at its center. All geometric objects are shown in Figure B1. With knowledge of these two variables, a proof will be constructed to determine the radius of the circle, *R*, and the maximum vertical distance between the chord and the minor arc that is created, *h*, as a function of only these two variables. This information will then be used to help determine the departure size of a gas bubble.

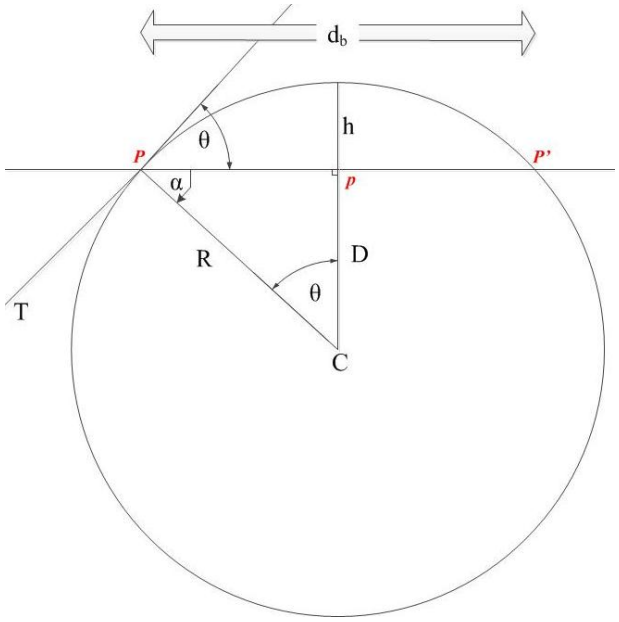

Figure B1: Geometry of interest. The only known quantities are θ and d_b. All other quantities will be used to determine the relationship between these variables and unknown variables R, D, and h.

In Figure B1, a circle (centered at C) is given, along with a chord (d_b) and a tangent line which intersects the circle at one of the ends of the chord. This intersection point is labeled *P*. Thus the angle between the tangent line and the chord is known. This is significant because the chord acts like a flat surface on which a gas bubble can sit. Depending on the contact angle, the volume of the sphere can be obtained from either from the section of the circle under the chord (for a wetting surface), or above the chord (for a non-wetting surface). The proof is constructed using the orientation presented above.

To begin, a radius is drawn from the center of the circle to point *P*, and is labeled '*R*'. By a similar method, another radius is drawn perpendicular to the chord, which divides its length into two separate lines, labeled *D* and *p*. A right triangle is formed by the points C, *P*, and *p*. A Geometric theorem states that when a tangent line passes through a circle's radius, the angles formed are right angles. By using this knowledge, all of the angles in the triangle are known. This process can be repeated on the opposite side of the chord at point *P'*. This creates two triangles with identical angles that share a side, *D*. This results in two triangles that are congruent by ASA triangle congruence.

With knowledge of the triangles congruence, this means that each of the sides have identical lengths. Since the pair of bases on the chord d_b must have the same length, they split the distance in half. Now, with one of the triangle's lengths known, the remaining lengths can be found. This is shown in the following equations.

$$\sin\theta = \frac{\frac{1}{2}d_b}{R} \qquad \tan\theta = \frac{\frac{1}{2}d_b}{D} \qquad h = R - D \qquad \text{(B0)}$$

Thus the following equations show the relationships between the base diameter and the contact angle with the circle radius (R) and cap height (h).

$$R = \frac{d_b}{2}\csc\theta \tag{B1}$$

$$D = \frac{d_b}{2}\cot\theta \tag{B2}$$

$$h = \frac{d_b}{2}(\csc\theta - \cot\theta) \tag{B3}$$

B.2 Force Balance on a Static Bubble (Wetting and Neutral Surface)

Force balance and mathematical model for static bubble departure prediction. Only the vertical-components of the forces are considered due to the direction of the surface tension force which exerts a net force in that direction only. The non-wetting surface was described in §*3.4: CO_2 Gas Departure within a DCFC*, thus the wetting and neutral surfaces are presented here.

Case 1: Wetting Surface ($\theta < 90°$)

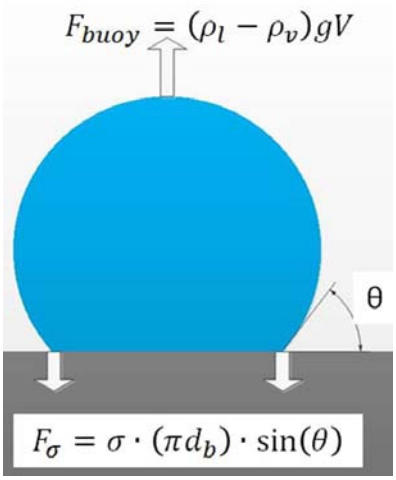

Figure B2: Free body diagram of a static bubble on a surface with a contact angle less than 90°

$$F_{buoy} = F_{\sigma} \tag{B4}$$

$$(\rho_l - \rho_v)Vg = \sigma(\pi d_b)\sin\theta \tag{B5}$$

$$d_b = \frac{(\rho_l - \rho_v)Vg}{\sigma\pi}\csc\theta \tag{B6}$$

If the contact angle between the liquid and the surface is less than 90°, then the volume of the gas bubble is equivalent to that of a sphere less the spherical cap that is defined by the diameter of the base which is a function of the contact angle only.

$$V = V_{sphere} - V_{cap} \tag{B7}$$

$$V = \frac{4}{3}\pi R^3 - \frac{1}{3}\pi h^2(3R - h) \tag{B8}$$

Where *R* and *h* are defined in §*B.1 Geometric Proof*, as the radius of a spherical volume and height of a spherical cap with a base diameter of $d_b$respectively. Note that both of these values are dependent solely on base diameter and contact angle as defined in Eq. B1 and B3. By substituting these relationships into the volume of the bubble, the volume on a flat surface can be determined

$$V = \frac{4}{3}\pi\left(\frac{d_b}{2}\csc\theta\right)^3 - \frac{1}{3}\pi\left[\frac{d_b}{2}(\csc\theta - \cot\theta)\right]^2\left[3\left(\frac{d_b}{2}\csc\theta\right) - \left(\frac{d_b}{2}\right)(\csc\theta - \cot\theta)\right] \tag{B9}$$

$$V = \frac{\pi}{3}\left(\frac{d_b}{2}\right)^3[4csc^3\theta - (\csc\theta - \cot\theta)^2(2\csc\theta + \cot\theta)] \tag{B10}$$

Substitute this relationship for the volume into Eq. B6 to determine the base diameter when the surface tension and buoyant forces are equivalent as a function of the contact angle.

$$d_b = \left(\frac{(\rho_l - \rho_v)g}{\sigma\pi}\csc\theta\right)\left(\frac{\pi}{3}\right)\left(\frac{d_b}{2}\right)^3 \times [4csc^3\theta - (\csc\theta - \cot\theta)^2(2\csc\theta + \cot\theta)] \quad \text{(B11)}$$

Therefore, after rearranging, the diameter of the base can be calculated by use of the following equation:

$$d_b^2 = \frac{24\sigma\sin\theta}{g(\rho_l - \rho_v)}[4csc^3\theta - (\csc\theta - \cot\theta)^2(2\csc\theta + \cot\theta)]^{-1} \quad \text{(B12)}$$

Insert the diameter of the base as calculated from Eq. B12 into Eq. B10 to determine the bubble volume at the moment of departure. Assuming that the bubble surface area would be a circular, the surface area covered by the particle would then be:

$$A_c = \frac{\pi d_b^2}{4} \quad \text{(B13)}$$

Case 2: Neutral Surface (θ = 90°)

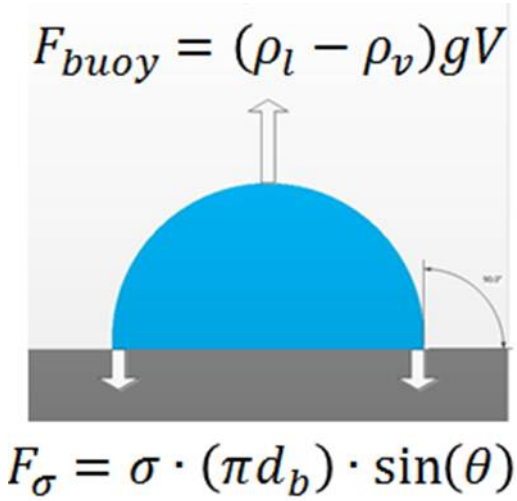

Figure B3: Free body diagram of a static bubble on a surface with a contact angle equal to 90°

$$F_{buoy} = F_{\sigma} \tag{B14}$$

$$(\rho_l - \rho_v)Vg = \sigma(\pi d_b) \tag{B15}$$

If the contact angle is 90° between the liquid and the surface, then the volume of the bubble is equal to half that of a sphere.

$$V = \frac{1}{2}\left[\frac{4}{3}\pi\left(\frac{d_b}{2}\right)^3\right] \tag{B16}$$

$$V = \frac{\pi d_b^3}{12} \tag{B17}$$

Insert the equation for the bubble volume into the force balance to determine the diameter of the base when surface tension and buoyant forces match and departure is set to begin.

$$(\rho_l - \rho_v)g\left(\frac{\pi d_b^3}{12}\right) = \sigma(\pi d_b) \tag{B18}$$

$$d_b^2 = \frac{12\sigma}{g(\rho_l - \rho_v)} \tag{B19}$$

Insert the diameter of the base as calculated from Eq. B19 into Eq. B17 to determine the bubble volume at the moment of departure. Assuming that the bubble surface area would be a circular, the surface area covered by the particle would be:

$$A_c = \frac{\pi d_b^2}{4} \tag{B20}$$

Appendix C: MATLAB Program for Determining the Volume of a Static Gas Bubble in Equilibrium

```
% Input the surface tension coefficient
sigma = 0.2; % N/m
% Input the density of the molten carbonate bubble
rho = 2000; % kg/m3
% This program determines the geometry at the point departure of a
% gas bubble begins, and can output any of the required data geometries
%-----------------------------------------%
g=9.81; % m/s2
for theta = 0:1:180,
    count = (theta)/1+1; % Implement a counter
    THETA(count)=theta;
    if theta == 0,
        V(count) = 0.0;
    elseif theta < 90,
        t=theta;
        % Determine the departure radius
        angle=4*(cscd(t)^3)-((cscd(t)-cotd(t))^2)*(2*cscd(t)+cotd(t));
         d(count)=sqrt(24*sigma*sind(t)/angle/rho/g);
         % Calculate the departure Volume
         V(count)=pi*(d(count)^3)*angle/24;
         % Departure Volume in cubic millimeters
         V_mm(count)=(1.0e9)*V(count);
         A_base_mm(count)=pi*d(count)*d(count)*1e6;
         R_bubble_mm(count)=0.5*d(count)/sind(t)*1000;
    elseif theta == 90,
         % Determine the departure radius
         d(count)=sqrt(12*sigma/rho/g);
         % Output the volume at departure
         V(count)=(2/3*pi)*((0.5*d(count))^3);
         V_mm(count)=(1.0e9)*V(count);
         A_base_mm(count)=pi*d(count)*d(count)*1e6;
         R_bubble_mm(count)=0.5*d(count)/sind(t)*1000;
     elseif theta > 90,
         tc=180-theta;
         angle=((cscd(tc)-cotd(tc))^2)*(2*cscd(tc)+cotd(tc));
         % Determine the departure radius
         d(count)=sqrt(24*sigma*sind(tc)/rho/g/angle);
         % Output the volume at departure
         V(count)=pi/24*(d(count)^3)*angle;
         V_mm(count)=(1.0e9)*V(count);
         A_base_mm(count)=pi*d(count)*d(count)*1e6;
         R_bubble_mm(count)=0.5*d(count)/sind(t)*1000;
    end
end
% Change the second vector and y label to change the plotted variable
% plot(THETA,A_base_mm)
% For two different y axis
% you'll need to add the second axis title manually
plotyy(THETA,V_mm,THETA,A_base_mm)
xlabel('Contact Angle (\circ)')
ylabel(Gas Bubble Departure Volume (mm^3)')
% Go to Edit > Figure Properties to change the style of the line
grid on
```

References

ANSYS FLUENT
2009 ANSYS FLUENT 12.0 Theory Guide. Providence, RI: ANSYS Inc.

Botsaris, Gregory D., and Yuli M. Glazman, eds.
1989 Surfactant Science Series, vol. 32: Interfacial Phenomena in Coal Technology. New York: Marcel Dekker Inc.

Cao, Dianxue, Yong Sun, and Guiling Wang
2007 Direct Carbon Fuel Cell: Fundamentals and Recent Developments. Journal of Power Sources, 167(2007):250-257.

Chen, C.C., and J. R. Selman
2010 Mathematical Model of Carbon Corrosion in a Direct Carbon Fuel Cell. ECS Transactions, 28(16):31-43.

Chen, Mingming, Chengyang Wang, Xiaomeng Niu, Shuo Zhao, Jian Tang, and Bin Zhu
2012 Carbon Anode in in Direct Carbon Fuel Cell. International Journal of Hydrogen Energy, 35(2010):2732-2736.

Cherepy, Nerine J., Roger Krueger, Kyle J Fiet, Alan F. Jankowski, and John F. Cooper
2005. Direct Conversion of Carbon Fuels in Molten Carbonate Fuel Cell. Journal of the Electrochemical Society 152(1):A80-A87.

Cooper, John F.
2004. Direct Conversion of Coal and Coal-Derived Carbon in Fuel Cells. ASME Conf. Proc. 2004, 375 (2004), DOI:10.1115/FUELCELL2004-2495

Faghri, Amir, and Yuwen Zhang
2006. Transport Phenomena in Multiphase Systems. Boston: Academic Press.

Fenghour, A., W. A. Wakeham, and V. Vesovic
1998 The Viscosity of Carbon Dioxide. Journal of Physical Chemistry Ref. Data 27(1):31-44.

Hirt, C. W. and B. D. Nichols
1981 Volume of Fluid Method for the Dynamics of Free Boundaries. Journal of Computational Physics 39(1):201-225.

Hong, Suk-Gi andJ. Robert Selman
2004 Wetting Characteristics of Carbonate Melts under MCFC Operating Conditions. Journal of the Electrochemical Society, 151(1):A77-A84.

Jones, S.F., G.M. Evans, and K.P. Gavin
1999. Bubble Nucleation from Gas Cavities – a Review. Advances in Colloid and Interface Sciences 80:27-50.

Kojima, Toshikatsu, Yoshinori Miyazaki, Katsuhiro Nomura, and Kazumi Tanimoto
2008 Density, Surface Tension, and Electrical Conductivity of Ternary Molten Carbonate System LI_2CO_3-Na_2CO_3-K_2CO_3 and Methods for Their Estimation. Journal of the Electrochemical Society 155(7):F150-F156.

Li, Xiang, Zhonghua Zhu, Jiunling Chen, Roland De Marco, Andrew Dicks, John Bradley, and Gaoqing Lu
2009 Surface Modification of Carbon Fuels for Direct Carbon Fuel Cells. Journal of Power Sources 186(2009):1-9.

Li, Xiang, Zhounghua Zhu, Roland De Marco, John Bradley and Andrew Dicks
2010a Evaluation of Raw Coals as Fuels for Direct Carbon Fuel Cells. Journal of Power Sources 195:4051-4058.
2010b Modification of Coal as a Fuel for the Direct Carbon Fuel Cell. Journal of Physical Chemistry 114:3855-3862.

Muthuvel, M., X. Jin, and GG Botte
2009 Exploratory Fuel Cells - Exploratory Fuel Cells: Direct Carbon Fuel Cells. *In* Encyclopedia of Electrochemical Power Sources. Jürgen Garche ed. Pp. 158-171. Elsevier: Academic Press, Spain.

Phan, Hai Trieu, Nadia Caney, Philippe Marty, Stéphane Colasson, and Jérôme Gavillet
2009 How Does Wettability Influence Nucleate Boiling? C.R. Mecanique 337:251-259.

Pierson, Hugh O.
1993 Handbook of Carbon, Graphite, Diamond, and Fullerenes: Properties, Processing and Applications. Park Ridge, NJ: Noyes Publications

Pioro, I. L.
1999 Experimental Evaluation of Constants for the Rohsenow Pool Boiling Correlation. International Journal of Heat and Mass Transfer
42(1999):2003-2013.

Rohsenow, W. M.
1952 A Method of Correlating Heat-Transfer Data for Surface Boiling of Liquids. Transactions of the American Society of Mechanical Engineers,
74:969-976.

Takata, Yasuyuki, Sumitomo Hidaka, and Masamichi Kohno
2010 Effect of Surface Wettability on Pool Boiling - Enhancement by Hydrophobic Coating. International Journal of Air-Conditioning and Refrigeration, 18(1):1-5.

Vutekakis, D. G., D. R. Skidmore, and H. J. Byker
1987 Electrochemical Oxidation of Molten Carbonate-Coal Slurries. Journal of the Electrochemical Society, 134(12):3027-3035.

Webb, Ralph L.
1994 Principles of Enhanced Heat Transfer. New York: John Wiley & Sons.